Deep Realistic Extragalactic Model (DREaM) Galaxy Catalogs: Predictions for a *Roman* Ultra-Deep Field

Nicole E. Drakos,[1] Bruno Villasenor,[1] Brant E. Robertson,[1] Ryan Hausen,[2] Mark E. Dickinson,[3]
Henry C. Ferguson,[4] Steven R. Furlanetto,[5] Jenny E. Greene,[6] Piero Madau,[7] Alice E. Shapley,[8]
Daniel P. Stark,[9] and Risa H. Wechsler[10, 11, 12]

[1]*Department of Astronomy and Astrophysics, University of California, Santa Cruz, 1156 High Street, Santa Cruz, CA 95064, USA*
[2]*Department of Computer Science and Engineering, University of California, Santa Cruz, 1156 High Street, Santa Cruz, CA 95064, USA*
[3]*National Optical-Infrared Astronomy Research Laboratory, 950 North Cherry Avenue, Tucson, AZ 85719, USA*
[4]*Space Telescope Science Institute, 3700 San Martin Drive, Baltimore, MD 21218, USA*
[5]*Department of Physics and Astronomy, University of California, Los Angeles, CA 90024, USA*
[6]*Department of Astrophysical Sciences, Princeton University, Princeton, New Jersey 08544, USA*
[7]*Department of Astronomy and Astrophysics, University of California, Santa Cruz, 1156 High Street, Santa Cruz, CA 95064, USA*
[8]*Department of Physics and Astronomy, University of California, Los Angeles, 430 Portola Plaza, Los Angeles, CA 90095, USA*
[9]*Department of Astronomy, Steward Observatory, University of Arizona, 933 North Cherry Avenue, Tucson, AZ 85721, USA*
[10]*Department of Physics, Stanford University, 382 Via Pueblo Mall, Stanford, CA 94305, USA*
[11]*Kavli Institute for Particle Astrophysics and Cosmology, Stanford University, Stanford, CA 94305, USA*
[12]*SLAC National Accelerator Laboratory, Menlo Park, CA 94025, USA*

ABSTRACT

In the next decade, deep galaxy surveys from telescopes such as the *James Webb Space Telescope* and *Roman Space Telescope* will provide transformational data sets that will greatly enhance the understanding of galaxy formation during the epoch of reionization (EoR). In this work, we present the Deep Realistic Extragalactic Model (DREaM) for creating synthetic galaxy catalogs. Our model combines dark matter simulations, subhalo abundance matching and empirical models, and includes galaxy positions, morphologies, and spectral energy distributions (SEDs). The resulting synthetic catalog extends to redshifts $z \sim 12$, and galaxy masses $\log_{10}(M/M_\odot) = 5$ covering an area of 1 deg^2 on the sky. We use DREaM to explore the science returns of a 1 deg^2 *Roman* UDF, and to provide a resource for optimizing ultra-deep survey designs. We find that a *Roman* UDF to $\sim 30\,m_{\rm AB}$ will potentially detect more than 10^6 $M_{\rm UV} < -17$ galaxies, with more than 10^4 at redshifts $z > 7$, offering an unparalleled dataset for constraining galaxy properties during the EoR. Our synthetic catalogs and simulated images are made publicly available to provide the community with a tool to prepare for upcoming data.

Keywords: galaxies: high redshift – galaxies: evolution – cosmology: reionization

1. INTRODUCTION

The basic picture of galaxy formation is well-established. Galaxies first form within the gravitational potential wells of dark matter halos, and continue to grow through the accretion of surrounding matter. Galaxies eventually produce enough radiation to ionize the intergalactic medium (IGM)—an epoch called reionization (for a review see Robertson et al. 2010; Stark 2016). Constraints from a variety of probes, including

the cosmic microwave background (CMB; e.g. Planck Collaboration et al. 2018) and quasar absorption lines (e.g. Becker et al. 2015), indicate that reionization happens between $z = 6$ and $z = 9$. If galaxies dominate the contribution of photoionizing radiation, the cosmic star-formation rate density (CSFRD) provides a measure of the photoionizing rate. Observing high-redshift galaxies, to study galaxy formation and their role in reionization, requires very deep imaging.

Extragalactic ultra-deep surveys such as the Hubble Ultra-Deep Field (HUDF; e.g. Beckwith et al. 2006) and Hubble Frontier Fields (HFF; e.g. Lotz et al. 2017) have detected galaxies to magnitudes $m_{\rm AB} \sim 30$ and have

begun to measure galaxy properties out to redshifts of $z \sim 10$. However, there are still many open questions at these high redshifts including the emergence of quiescent galaxies, the evolution of the UV luminosity function (UVLF; e.g. Bouwens et al. 2021), and the exact timeline and mechanism of cosmic reionization (e.g. Bunker et al. 2004; Finkelstein et al. 2012; Robertson et al. 2015). Upcoming telescopes, including *James Webb Space Telescope (JWST)* and the *Nancy Grace Roman Telescope (Roman)* will produce a large influx of data in the coming years that will greatly advance our understanding of galaxy evolution in the epoch of reionization (EoR). Given that *Roman* is scheduled to launch in a few years, the purpose of this paper is to examine the science returns of an ultra-deep survey with *Roman*.

The main advantage of *Roman* compared to other space telescopes is its wide field of view (FOV); the *Roman* Wide-Field Instrument (WFI) FOV is more than 100x larger than *HST*'s WFC3 and *JWST*'s NIRCam. This large area will increase the number of detected galaxies, discover bright and rare sources, reduce cosmic variance, and probe the environment around galaxies and active galactic nuclei (AGN) at unprecedented redshifts. As outlined in Koekemoer et al. (2019), a potential Roman Ultra-Deep Field (UDF) survey could cover $\sim 1\,\mathrm{deg}^2$ and image to $m_{\mathrm{AB}} \sim 30$ in ~ 600 hours of exposure time per filter. This survey would elucidate the properties of the dominant ionizing sources at the time of reionization, allow tests for variations in the high-z faint-end slope of the UVLF with environment, and likely provide the first galaxy clustering constraints at early times for faint galaxies.

A prerequisite to understanding in detail what a *Roman* UDF will be able to detect is accurate modeling of the expected observations. In particular, synthetic galaxy catalogs are useful for predicting the science returns of an upcoming survey, to test analysis tools, and identify potential observational biases (e.g. Williams et al. 2018; Yung et al. 2019a; Korytov et al. 2019; Behroozi et al. 2020; Somerville et al. 2021). To make accurate predictions, the quality and complexity of synthetic observations needs to increase with expanding theoretical and observational knowledge. This work presents the Deep Realistic Extragalactic Model (DREaM), a model for generating synthetic galaxies out to redshifts past the EoR. DREaM accurately reproduces a wide range of theoretical and observational trends, including stellar mass functions (SMFs), and the CSFRD. We use DREaM to create synthetic data for a potential *Roman* UDF, to provide synthetic catalogs for the community to help develop analysis and pipeline

tools, and quantify the potential scientific returns of a *Roman* UDF.
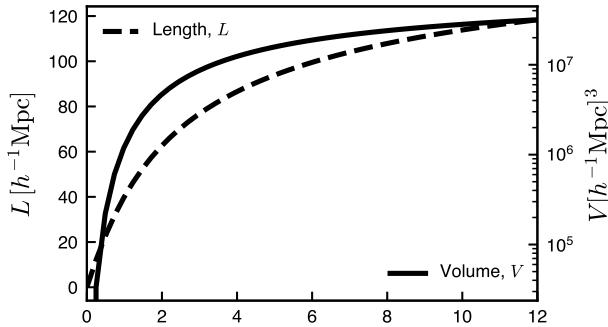
To accurately capture the environment around each galaxy, we begin with dark matter simulations, and then create an observed lightcone by stitching together the discrete simulation outputs. The outline of this paper is as follows: an overview of DREaM is given in Section 2. The underlying dark matter simulations, and the method for assigning galaxies to dark matter halos is given in Section 3, and the process of creating the observed lightcone in Section 4. The galaxy morphologies and spectral energy distributions (SEDs) are assigned as outlined in Sections 5 and Section 6, respectively. The resulting star formation history of the universe is discussed in Section 7, and preliminary predictions for the science returns of a $1\,\mathrm{deg}^2$ UDF with *Roman* are given in Section 8. Finally, the implications of this study and future work are discussed in Section 9.

2. OVERVIEW OF METHODS

While knowledge of galaxy distributions and properties comes primarily from observations, dark matter structure is typically studied through numerical simulations. The galaxy–halo connection describes how visible galaxies relate to the underlying dark matter structure (for a recent review see Wechsler & Tinker 2018). Many different approaches have been used to link halo properties to galaxies, including hydrodynamical simulations (e.g. Katz & Gunn 1991; Katz 1992; Vogelsberger et al. 2014), semianalytic models (SAMs) (e.g. White & Frenk 1991; Kauffmann et al. 1993; Somerville & Primack 1999; Guo et al. 2013), halo occupation distribution models (HOD models; Jing et al. 1998; Berlind & Weinberg 2002; Wechsler et al. 2002), abundance matching (AM; e.g. Kravtsov et al. 2004; Conroy et al. 2006; Vale & Ostriker 2006), and machine learning (e.g. Jo & Kim 2019; Moster et al. 2020; Wechsler et al. 2021). These different techniques range from physically driven, computationally expensive approaches to empirical models designed to reproduce known observational trends.

More physically based approaches are theoretically more predictive than empirical models. However, both hydrodynamical simulations and SAMs typically struggle to reproduce observed trends to the same accuracy as empirical models (which match observations by construction).[1] Therefore, to successfully reproduce observational trends (including luminosity functions, star formation histories, and galaxy clustering), synthetic

---

[1] Though there has been success with the Santa Cruz SAM (Somerville & Davé 2015) in making predictions for upcoming *JWST* observations (Yung et al. 2019a,b, 2020b,a).

Figure 1. Comoving transverse size, L, and volume, V, of a survey with a square $1\,\mathrm{deg}^2$ field of view. We calculate distances assuming a Planck 2018 cosmology (Planck Collaboration et al. 2018). A redshift of $z = 10$ corresponds to a comoving size of $\sim 115\mathrm{Mpc}h^{-1}$ in the transverse direction.

galaxy catalogs most commonly use empirical models that place galaxies in dark matter structure using AM related methods (e.g. Moster et al. 2018; DeRose et al. 2019; Behroozi et al. 2019, 2020; DeRose et al. 2021) or HOD models (e.g. van den Bosch et al. 2005; Zu & Mandelbaum 2015).

For the synthetic catalog presented in this work, we begin with dark matter simulations, and then use sub-halo abundance matching (SHAM) to model the galaxy–halo connection, as outlined in Section 3. The main advantages to this approach are that by beginning with dark matter simulations, we can accurately capture the large-scale structure, and provide host dark matter halo properties for each galaxy. SHAM methods reproduce the proper SMFs by construction, and are known to reproduce the spatial distribution of galaxies in the local Universe (e.g. Kravtsov et al. 2004; Reddick et al. 2013; Lehmann et al. 2017).

To simulate a $1\,\mathrm{deg}^2$ survey that extends past $z \sim 10$, we use a simulation volume with sides of comoving length $115\,h^{-1}\mathrm{Mpc}$. Fig. 1 shows the comoving transverse size of a patch of sky covering $1\,\mathrm{deg}^2$ as a function of redshift, and the corresponding volume of the survey. To reach the desired depth of the synthetic realization, we tile 60 boxes in the line-of-sight direction, as detailed in Section 4.1.

When constructing synthetic observations from simulations, the discrete time snapshots of the simulations need to be related to the observable sky, in which the distance of the object corresponds to its observed time. This relation between simulation data and the observable sky can be achieved by creating a lightcone. Our lightcone pipeline is described in detail in Section 4, but, in brief, given merger histories for each halo we calculate if, and at which time, each halo crosses the ob-

servers past lightcone. If the position of the galaxy on the lightcone falls within the survey volume, the galaxy is included in our synthetic catalog.

After creating the lightcone, we assign galaxy morphological properties and SEDs in a manner similar to the phenomenological model from Williams et al. (2018). Details of these procedures are outlined in Sections 5, and Section 6. We use the publicly available Flexible Stellar Population Synthesis (FSPS; Conroy et al. 2009; Conroy & Gunn 2010) code to generate galaxy SEDs and calculate galaxy fluxes in each of the proposed *Roman* filters.

A summary of the methods used to generate the synthetic catalogs is shown in Fig. 2. Section 3.1 describes the underlying dark matter simulation and creation of the halo catalog. Sections 3.2 and 4 outline the SHAM and lightcone procedure, respectively. We assign morphologies and SEDs to the galaxies as described in Sections 5 and 6, respectively). Then, Section 8 outlines the *Roman* photometry.
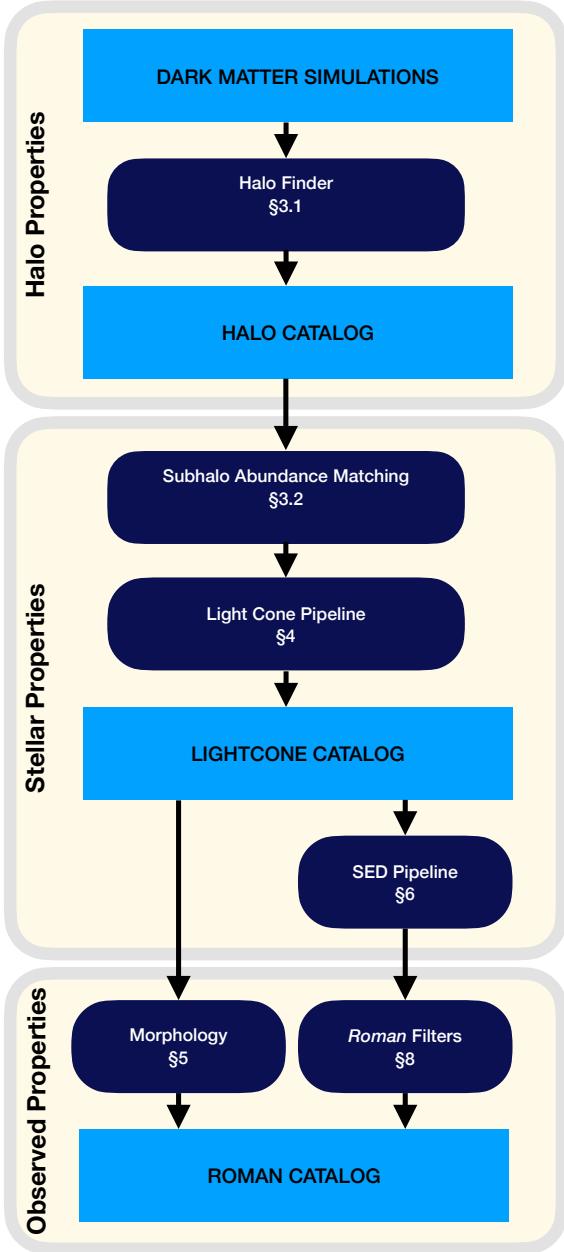
3. GENERATING SYNTHETIC GALAXIES

As described above, we begin our catalog by running dark matter only simulations, and then use SHAM to assign stellar masses, resulting in halo catalogs with corresponding galaxy masses for every simulation time output. This section describes the underlying dark matter simulations, halo catalogs, and SHAM procedure. In the following section, we use these galaxies to create a lightcone realization of the catalog. We treat host halos and their subhalos (i.e. halos that exist inside a larger halo as a self-bound structure) separately, and use the term "halo" to refer to both host and subhalos.

3.1. *Dark matter simulation*

We use a Planck 2018 cosmology (Planck Collaboration et al. 2018, $\Omega_b = 0.04893$, $\Omega_0 = 0.3111$, $\Omega_\Lambda = 0.6889$, $H_0 = 67.66\,\mathrm{km/s/Mpc}$, $\sigma_8 = 0.8102$ and $n_s = 0.9665$), with a box size of $115\,h^{-1}\mathrm{Mpc}$ and $N = 2048^3$ particles. This corresponds to a particle mass of $1.5 \times 10^7 M_\odot h^{-1}$, The initial conditions are created using MUSIC (Hahn & Abel 2011), and the simulations are run in GADGET-2 (Springel 2005), with a softening length of 1.13 comoving $h^{-1}\mathrm{kpc}$. The simulation outputs are shown in Fig. 3. We generate halo catalogs and merger trees using ROCKSTAR (Behroozi et al. 2013a) and CONSISTENT TREES (Behroozi et al. 2013b). We define halo masses using the Bryan & Norman (1998) virial definition. Halos are required to have at least 20 particles, which corresponds to a minimum mass of $8.50 M_\odot h^{-1}$.

3.2. *Galaxy masses*

DREaM

Figure 2. Overview of methods used to create the *Roman* DREaM galaxy catalog, with the corresponding paper sections labeled. The galaxy catalog is based on a dark matter simulation. SHAM is used to assign galaxy masses to each dark matter halo, and then galaxy properties are assigned using empirical relations. Data products are shown with light blue rectangles, and pipelines are shown with dark blue ovals. The SED pipeline is shown in more detail in Fig. 9.

Given the halo lightcone catalog constructed in Section 3, we assign a galaxy stellar mass, $M_{\rm gal}$, to each halo. The SHAM procedure we use can be expressed mathematically as:

$$\int_x^\infty n(x', z)\mathrm{d}x' = \int_{M_{\rm gal}}^\infty \phi(M'_{\rm gal}, z)\mathrm{d}M'_{\rm gal} \qquad (1)$$

where $\phi(M_{\rm gal}, z)$ is the SMF (i.e. the comoving number density of galaxies per unit galaxy mass, per unit redshift), and $n(x)$ is the number density of halos as a function of some mass proxy, x.
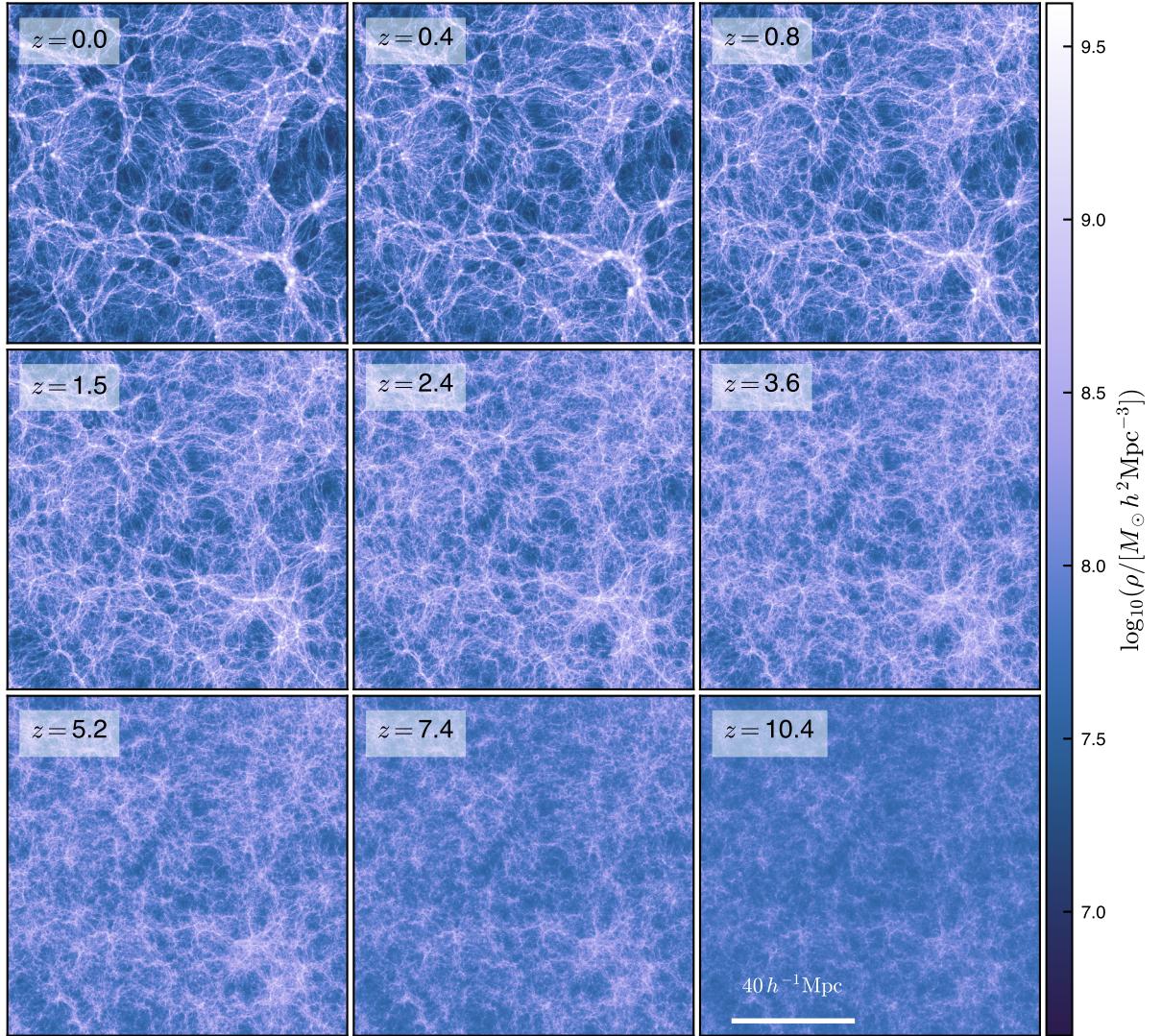
In the simplest formulation of SHAM, galaxy mass is directly mapped to halo mass. However, subhalo properties at the time of accretion are a better indicator of galaxy mass, since as subhalos undergo tidal stripping, they lose a significant amount of dark matter before the galaxy is disrupted (e.g. Conroy et al. 2006; Vale & Ostriker 2006). There are many different choices of mass proxies, and each of these choices produces slightly different spatial distributions of galaxies. We adopt the peak of the maximum circular velocity over the entire merger history, $V_{\rm peak}$, as the halo mass proxy, because SHAM with $V_{\rm peak}$ as the mass proxy is known to reproduce the small scale clustering of galaxies (Reddick et al. 2013; Hearin et al. 2013; Lehmann et al. 2017; Campbell et al. 2018).

We use the SMFs from Williams et al. (2018), which are continuously evolving double-Schechter functions for both star-forming and quiescent galaxies out to redshifts $z > 10$. By construction, these SMFs match observational constraints at low redshifts ($z \leq 4$), and reproduce known UVLFs when convolved with the distribution of rest-frame UV magnitudes, $M_{\rm UV}$, i.e.:

$$\Phi_{\rm UV}(M_{\rm UV}, z)$$
$$= \int_0^\infty \phi(M'_{\rm gal})\mathcal{N}[M_{\rm UV}, \bar{M}_{\rm UV}(M'_{\rm gal}, z), \sigma_{\rm UV}]\mathrm{d}M'_{\rm gal} \ ,$$
$$(2)$$

where $\mathcal{N}[M_{\rm UV}, \bar{M}_{\rm UV}(M_{\rm gal}, z), \sigma_{\rm UV}]$ is a normal distribution centered on the average UV magnitude $\bar{M}_{\rm UV}$ and $\sigma_{\rm UV}$ is the scatter in the $M_{\rm gal}$–$\bar{M}_{\rm UV}$ relation. Williams et al. (2018) provide a relation to describe the $M_{\rm gal}$–$\bar{M}_{\rm UV}$ relation and scatter, which we use to model our galaxies (see Section 6.4).

For redshifts $z \leq 4$, Williams et al. (2018) fit the double-Schechter function to the data from Tomczak et al. (2014). For quiescent galaxies (QGs), above $z \sim 4$ the Schechter parameters are extrapolated to higher redshifts. This extrapolation is in agreement with the few constraints for quiescent galaxies at $z > 3.5$. For star-forming galaxies (SFGs), the high redshift SMFs are inferred from UVLFs. Specifically, Williams et al. (2018)

Figure 3. Cosmological N-body simulation with a box size of $115h^{-1}$Mpc. The figure shows the projected mass density at various redshifts (as labeled), in a 7 Mpc/h slice in the radial direction. These simulations serve as the basic input for finding halos and modeling the galaxy population.

used data from Bouwens et al. (2015) for $4 \le z \le 8$ and from Oesch et al. (2018) at $z = 10$ to fit the SMF in Equation (2). Beyond $z \sim 10$, the SMFs for the SFGs are extrapolated.

We perform SHAM on the halo catalogs using the SMFs described above. Specifically, given N halos, we first find the minimum galaxy mass, $M_{\min}$, such that $N_{\mathrm{gal}}(> M_{\min}) = N$, where

$$N_{\mathrm{gal}}(> M_{\min}) = V \int_{M_{\min}}^{\infty} \phi(M'_{\mathrm{gal}}) \mathrm{d}M'_{\mathrm{gal}} \ , \qquad (3)$$

and V is the comoving volume of the simulation. We then sample N galaxy masses from the SMF above

$M_{\min}$. Finally, we rank-order the galaxy masses and assign galaxy masses to halos (such that the halo with the largest V_{peak} value gets the largest galaxy mass).

Scatter is commonly introduced in the relation between galaxy and halo properties by either deconvolving the SMF (e.g. Behroozi et al. 2010) or by directly adding scatter to the stellar masses, re-ranking, and iteratively solving for the galaxy mass (Hearin et al. 2013). Since our main goals are not to reproduce the observed scatter in the stellar-mass–halo-mass (SMHM) relation, we did not include scatter in the SHAM procedure. As illustrated in Section 4.3, we are able to produce realistic

statistical galaxy properties, such as galaxy clustering with our approach.

We classify each galaxy as either a star-forming galaxy (SFG) or a quiescent galaxy (QG) by randomly generating a number and comparing it to the probability a galaxy of that mass is star-forming, as calculated from the SMFs. This method does ignore a possible correlation between SFR and mass accretion histories (e.g. Behroozi et al. 2019), which could potentially impact galaxy clustering with SFR. In particular, QGs are more likely to be found in denser environments (e.g. Kauffmann et al. 2004; Kimm et al. 2009). Finally we remove all galaxies from the catalog with $M_{\rm gal} < 10^5 M_\odot$. As shown in Section 8, the fraction of detectable galaxies below this mass is zero for redshifts $z > 1$.[2]

4. LIGHTCONE PIPELINE

Thus far we have created halo catalogs with galaxy masses at different time outputs. In this section we detail how we construct a lightcone from these discrete snapshots to create a $1\,{\rm deg}^2$ survey of galaxies (the "Lightcone Catalog"). In Section 4.3, we demonstrate that we are able to reproduce essential statistical properties of galaxy populations with this Lightcone Catalog.

4.1. *Lightcone crossing*

For this work, we consider a survey with a 1 deg² field of view. To reach redshifts $z \gtrsim 10$, we tile 60 boxes in the line-of-sight direction. This corresponds to a maximum redshift of 13 and a comoving distance of 6900 Mpc. As in Bernyk et al. (e.g. 2016), to avoid the replication of structures viewed by the observer, we randomly translate, reflect, and permute the axes of every tiled simulation box. We construct the halo lightcone by finding where each halo first crossed the observers past lightcone (i.e., the location at which light has had just enough time to reach the observer). Technical aspects associated with this procedure are outlined extensively in the literature (e.g. Evrard et al. 2002; Blaizot et al. 2005; Kitzbichler & White 2007; Merson et al. 2013; Bernyk et al. 2016; Smith et al. 2017; Korytov et al. 2019). In this section, we closely follow the procedure used to generate the CosmoDC2 sky catalog for *LSST* (Hollowed 2019; Korytov et al. 2019).

We assume that the observer is at the origin of the coordinate system $(x, y, z) = (0, 0, 0)$. For each tiled box,

we begin by placing all the host halos on the lightcone. For every host halo in snapshot j, we determine its position in the subsequent snapshot, r_{j+1}. We extrapolate the halo position from j by assuming constant velocity to find its extrapolated position in snapshot $j + 1$, $r_{j+1,\rm extrap}$. If the halo did not have a descendant located in snapshot $j + 1$, we set $r_{j+1} = r_{j+1,\rm extrap}$. Otherwise, we use:

$$r_{j+1} = r_{j+1,\rm extrap} + {\rm int}\left(\frac{r_{j+1,\rm extrap} - r_{j+1,\rm desc}}{L}\right) \times L \ , \tag{4}$$

where L is the length of the simulation box, int represents integer, and $r_{j+1,\rm desc}$ is the position of the descendant in snapshot $j + 1$. This approach allows the halo to cross the edge of the simulation box between snapshots j and $j + 1$, and thus r_{j+1} might be outside the domain of the tiled box. In these cases, we also consider the scenario where the halo crosses the lightcone on the other side of the box; i.e., we apply periodic boundary conditions, such that

$$\begin{aligned} r_{j+1}^p &= r_{j+1} \bmod L \\ r_j^p &= r_j + (r_{j+1}^p - r_{j+1}) \ , \end{aligned} \tag{5}$$

to allow the halo to cross the observer lightcone between positions r_j^p and r_{j+1}^p.

Given the positions r_j and r_{j+1} for each host halo, we calculate the time the halo would cross the past lightcone, t_e (Equations 27-29 in Korytov et al. 2019). If the halo crosses between the snapshot times t_j and t_{j+1}, we calculate the position on the lightcone, r_e from:

$$\begin{aligned} v_{\rm lin} &= (r_{j+1} - r_j)/(t_{j+1} - t_j) \\ r_e &= r_j + v_{\rm lin}(t_e - t_j) \ . \end{aligned} \tag{6}$$

We do not include any halos where r_e is beyond the domain of the tiled box.

The final step to generating the lightcone is to assign halo properties (e.g. mass and substructure) to each object. One approach to assigning halo properties is to allow the merger of halos to happen at a time randomly between the two snapshot (e.g. Smith et al. 2017). However, this approach will result in halos being double counted, and the lightcone needs to be carefully pruned. Since our simulations have very fine time resolution (500 snapshots between redshifts $z = 0$ and $z = 20$), we can avoid the technical difficulties and assumptions introduced by needing to prune the catalog, and follow the same approach from Korytov et al. (2019). Specifically, every halo that crosses the lightcone between snapshots j and $j+1$ is assigned properties from snapshot j. When including the substructure, we ensure subhalos have the same position and velocity offset from the host as in snapshot j.

---

[2] Though faint high-redshift galaxies can also be detected through galaxy lensing, we expect this number to be very low for low-mass galaxies. For example, Kikuchihara et al. (2020) used gravitational lensing techniques to detect very faint drop out galaxies in the HFFs to redshifts $z \sim 6$, and detected galaxies with $M_{\rm gal} > 10^6 M_\odot$

4.2. Survey volume

Given the lightcone catalog consisting of halo properties, galaxy masses, and positions, we cut out a wedge in the survey volume corresponding to $1 \deg^2$. Following Bernyk et al. (2016), we convert the comoving (x, y, z) positions of each galaxy to an angular position as follows:

$$
d = \sqrt{x^2 + y^2 + z^2}
$$
$$
\mathrm{RA} = \frac{360}{2\pi} \arctan(y/x) \quad (7)
$$
$$
\mathrm{Dec} = \frac{360}{2\pi} \arcsin(z/d)
$$

We only consider galaxies with RA < 1 deg and Dec < 1 deg, and then center the galaxies on $(\mathrm{RA}, \mathrm{Dec}) = (0, 0)$.

Fig. 4 shows the resulting galaxy mass density as a function of position. The lightcone procedure results in a realistic distribution of galaxies that trace the underlying cosmic web. Since the survey will reach very deep distances, the survey is tiled in 6 rows, with each row showing 10 tiled boxes. The survey wedge is complete to a maximum distance of 6588 Mpc/h (which corresponds to a cosmological redshift of ~ 10.5); at higher reshifts, the angle of the survey is larger than the width of the simulation box. There are discontinuities in the galaxy density where the simulation boxes are tiled, which is a common feature for lightcones. As addressed in Bernyk et al. (2016), statistical properties of the galaxy catalog will be accurate on scales smaller than the box size.

4.3. Statistical properties of galaxy lightcone

To verify the lightcone pipeline results in a realistic galaxy population, we calculate the halo mass functions (HMFs), SMFs, stellar-to-halo mass relations (SHMRs) and galaxy clustering of the synthetic galaxy catalog.

4.3.1. Halo mass functions

To demonstrate the HMF of the halo lightcone catalog is correct, we plot the recovered HMF of host halos in Fig. 5. The theoretical curve is from the parameterization from Despali et al. (2016), and calculated using the HMF routine in COLOSSUS (Diemer 2018). The theoretical curve and simulation results agree very well. The catalog was constructed to be complete above galaxy masses $M_{\mathrm{gal}} = 10^5 M_\odot$, which corresponds to a halo mass limit of approximately $M_{\mathrm{halo}} \sim 10^{9.5} h^{-1} M_\odot$

4.3.2. Stellar mass functions and the stellar-to-halo mass relations

Additionally, we show the SMF of the lightcone catalog in Fig. 6 for both SFGs and QGs. For comparison, we show the volume-weighted average SMFs from Williams et al. (2018) (dotted lines), averaged over the redshift bin. The catalog is complete at all redshifts for galaxy masses greater than $10^5 M_\odot$. The galaxies in the lightcone agree with the SMFs from Williams et al. (2018), which verifies that the lightcone pipeline and abundance matching procedure reproduce realistic galaxy counts. As discussed in Section 3.2, producing the desired SMF is important for reproducing observed luminosity functions.

4.3.3. Galaxy clustering

Galaxy clustering is commonly described using the two-point correlation function (2PCF), $\xi(r)$, defined as

$$
\mathrm{d}P = n_g(r)[1 + \xi(r)]\mathrm{d}V \ , \quad (8)
$$

where $\mathrm{d}P$ is the excess probability above Poisson noise, $n_g(r)$ is the mean density of galaxies at separation r, and $\mathrm{d}V$ is the differential volume. In practice, the projected 2PCF, w_p, is often used. The 2PCF depends on the projected separation, r_p, and the line-of-sight separation, π:

$$
w_p = \int_{-\infty}^{\infty} \xi(r_p, \pi)\mathrm{d}\pi \approx 2 \times \int_0^{\pi_{\max}} \xi(r_p, \pi)\mathrm{d}\pi \ , \quad (9)
$$

where the second equality assumes isotropy. The upper limit, $\pi_{\max}$, needs to be chosen large enough to nullify the effect of peculiar velocities, but not so large that it creates artificial edge effects from the survey boundary. The optimal value for $\pi_{\max}$ depends on the underlying survey volume, but is typically in the range 40–80 Mpc (Zehavi et al. 2005; van den Bosch et al. 2013).

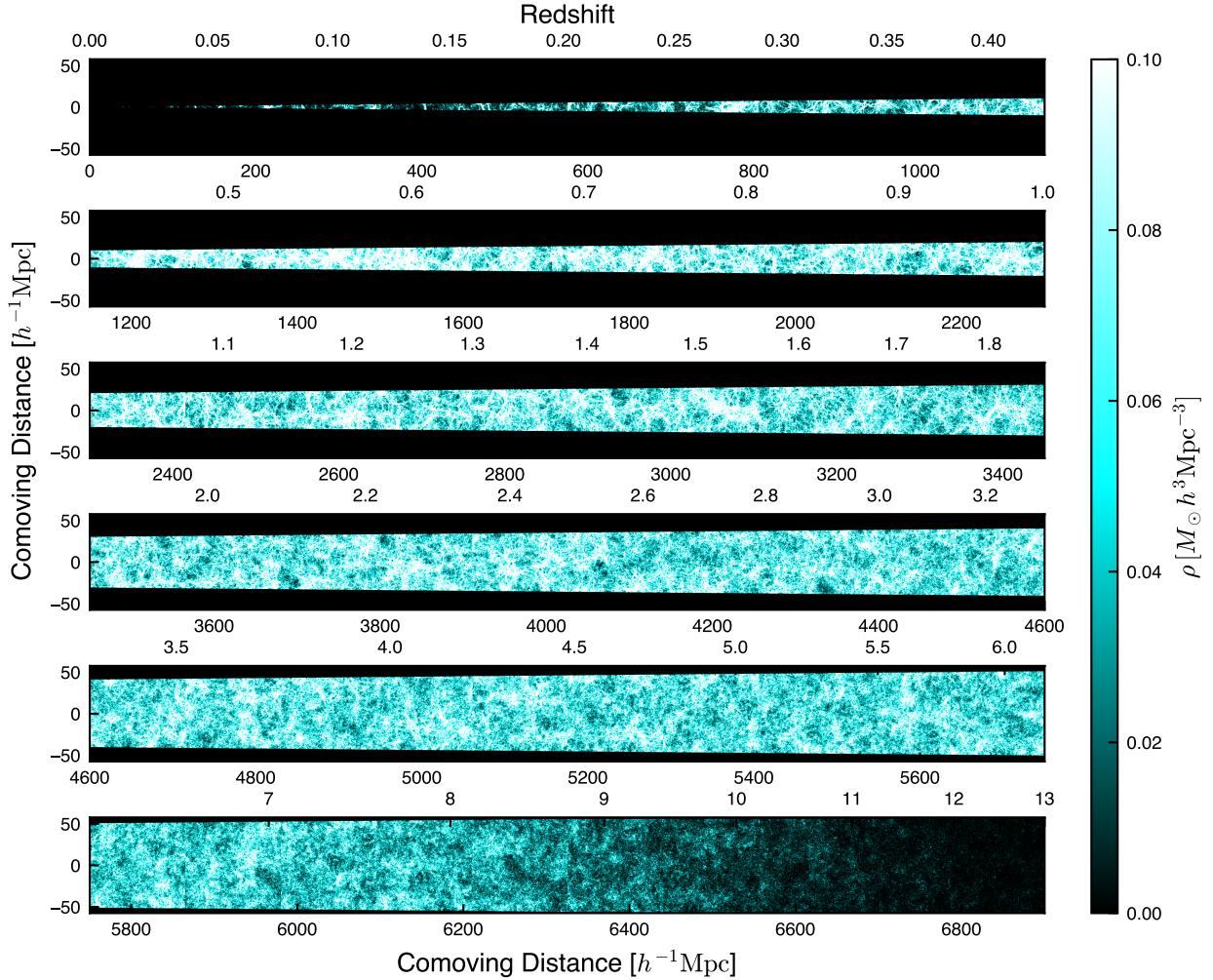We calculate ξ based on the commonly used Landy-Szalay estimator (Landy & Szalay 1993),

$$
\xi \approx \frac{DD - 2DR + RR}{RR} \ , \quad (10)
$$

where DD, DR and RR are normalized number of counts from data–data, data–random and random–random pairs. The random catalog contains 10^3 points per arcmin^2, with distances assigned such that the random catalog has the same redshift distribution as the synthetic catalog, i.e.,

$$
N(z_{\min} < z < z_{\max})
$$
$$
= \theta \sin(\theta) \int_{\chi(z_{\min})}^{\chi(z_{\max})} \chi^2 \int_{M_1}^{M_2} \phi(M, z(\chi))\mathrm{d}M\mathrm{d}\chi \quad (11)
$$

where θ is the survey angle, and ϕ is the Williams et al. (2018) SMF. Values for RA and Dec coordinates for each random galaxy were selected so that galaxies are distributed isotropically:

$$
\mathrm{RA} = r_1\theta
$$
$$
\mathrm{Dec} = \arcsin\left[2r_2 \sin\left(\frac{\theta}{2}\right)\right] \ . \quad (12)
$$

Figure 4. Mass density of galaxies in survey volume, with a field of view of $1 \deg^2$. The x-axis shows the cosmological redshift (top) and the comoving distance (bottom). We have plotted 10 tiled boxes in each row, for a total of 60 boxes to reach the desired redshift range. This figure demonstrates the depth and distribution of galaxies of a $1 \deg^2$ UDF.

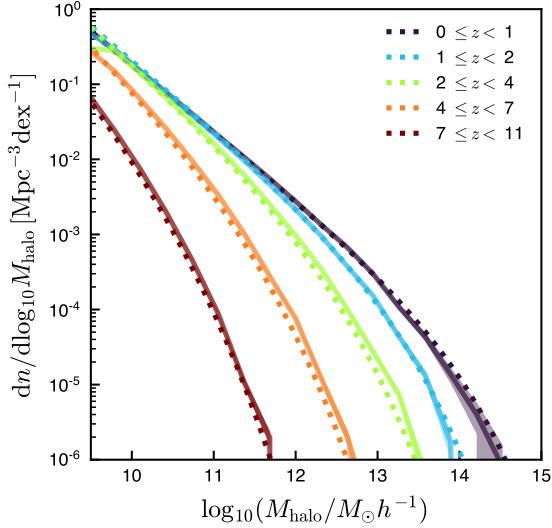where r_1, r_2 are random numbers selected uniformly between -0.5 and 0.5.

To measure the projected 2PCF we use the package Corrfunc (Sinha & Garrison 2020), with $\pi_{\mathrm{max}} = 60 \, h^{-1}$ Mpc. We estimate errors in the measured 2PCF by bootstrapping the galaxy catalog data with 200 subsamples. We present this measured 2PCF in Fig. 7, along with SDSS data for redshift $z \approx 0.1$ galaxies from Yang et al. (2012). To compare our synthetic catalog 2PCF to the data, we use galaxies in the redshift range $0.1 < z < 0.2$ within a $10 \deg \times 10 \deg$ survey. The low redshift clustering of the synthetic galaxies agree with observations within the $1 - \sigma$ error bars, indicating that the lightcone halo clustering is realistic.

5. GALAXY MORPHOLOGIES

Galaxy morphologies offer key insights into galaxy evolution, and are important for understanding observational systematics. We model all galaxies as Sérsic (1968) profiles with an index, n_s. Additionally, all galaxies are assigned a projected size R_{eff}, a projected axis ratio $q = b/a$, and a position angle (PA). We follow the morphological prescriptions from Williams et al. (2018)—which are based on the empirical distributions measured in *HST* images—with the exception of galaxy sizes.

5.1. *Size*
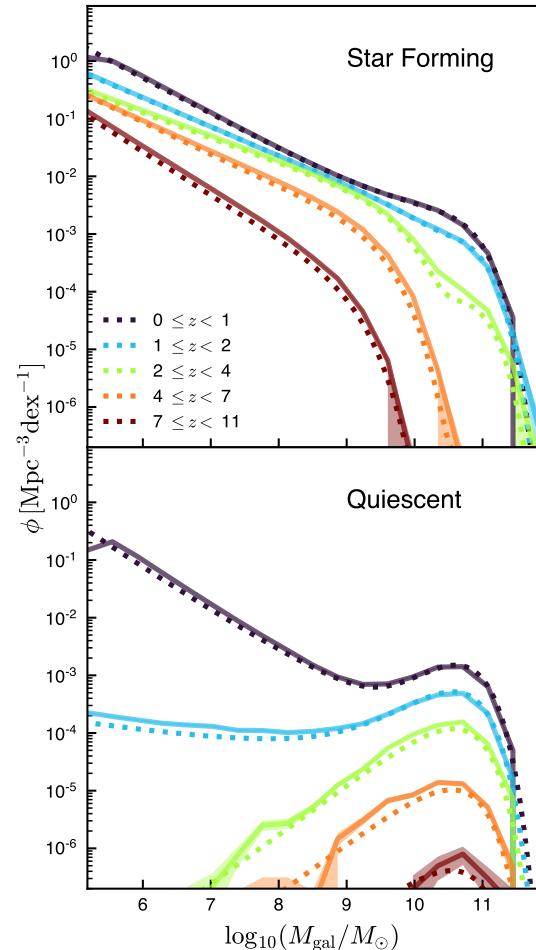
Figure 5. Expected HMF from the Despali et al. (2016) parameterization (dotted lines) compared to the host halos in the lightcone catalog (solid lines). The theoretical curve is the volume-weighted average over the redshift band. The lightcone catalog agrees with the expected HMF, verifying that the lightcone procedure reproduces the correct redshift and mass distribution of dark matter halos.

Galaxies sizes are known to decrease with increasing redshift at a fixed stellar mass (e.g. van der Wel et al. 2014; Shibuya et al. 2015; Curtis-Lake et al. 2016), typically evolving as

$$R_e \propto (1+z)^{-\alpha} \; , \qquad (13)$$

where R_e is the half-light radius. Further, SFGs and QGs evolve differently, with star-forming galaxies having lower values of α (e.g. van der Wel et al. 2014; Ma et al. 2018).[3] In addition to these observed trends, theoretical models commonly show a correlation between the size of a galaxy and that of its host dark matter halo (e.g. Mo et al. 1998; Kravtsov 2013; Jiang et al. 2019). Given that our synthetic catalog begins with the underlying dark matter structure, we assign galaxy sizes based on the dark matter halo sizes, and then test that the size–redshift–mass relation is consistent with current data.

---

[3] However, Miller et al. (2019) recently showed that differences between size trends for SFGs and QGs may disappear if you use r_{80}—the radius enclosing 80 % of stellar light—rather than R_e.
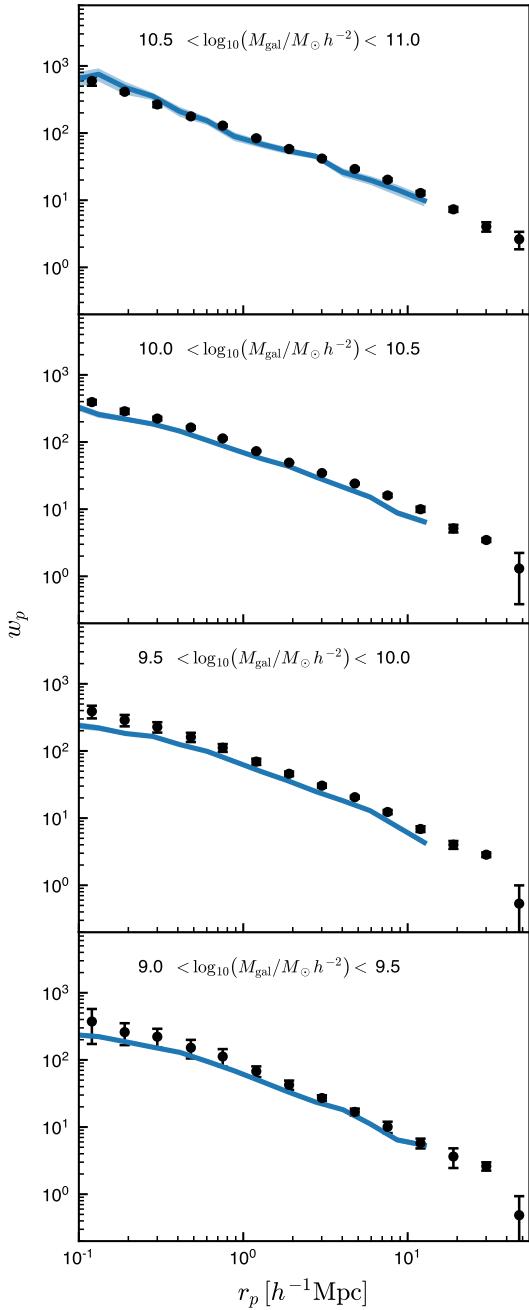
Figure 6. SMFs for the lightcone catalog. SFGs and QGs are shown in the top and bottom panels, respectively. The Williams et al. (2018) SMFs that were used in the abundance matching procedure are shown with dotted lines, calculated as a volume-weighted average over the redshift bin. The lightcone pipeline and abundance matching procedure reproduce the desired SMFs.

Specifically, we characterize the size of each galaxy as the half-light radius in the semi-major axis R_{eff}.[4] To assign R_{eff} to each galaxy, we use the relation between halo and galaxy size (e.g. Kravtsov 2013; Zanisi et al. 2020):

$$R_{\mathrm{eff}} = A \, R_{\mathrm{vir}}, \qquad (14)$$

---

[4] R_{eff} is related to the commonly used circularized half-mass radius, $R_{\mathrm{eff,circ}}$, by $R_{\mathrm{eff,circ}} = \sqrt{b/a} R_{\mathrm{eff}}$, where b/a is the minor-to-major axis ratio.

Figure 7. 2PCF in a $100 \deg^2$ lightcone catalog for all galaxies $0.1 < z < 0.2$ (lines). We estimate uncertainties in the synthetic catalog 2PCF by bootstrapping the data. In comparison, SDSS data from Yang et al. (2012), for galaxies at redshifts $z \approx 0.1$ are shown with black points. The agreement between the simulation and data shows that the lightcone catalog matches the observed galaxy clustering at low redshifts.

Table 1. Coefficients, A, for the $R_{\mathrm{eff}} - R_{\mathrm{vir}}$ relation (Equation 14) and the scatter σ_R; values are from Zanisi et al. (2020).

$\log_{10}(M_{\mathrm{gal}}/M_\odot)$	A (SFGs)	A (QGs)	σ_R
≤ 9.5	0.018	0.006	0.2
$(9.5, 10]$	0.019	0.007	0.2
$(10, 10.5]$	0.019	0.010	0.15
$(10.5, 11]$	0.019	0.011	0.15
$(11, 11.5]$	0.019	0.015	0.15
> 11.5	0.024	0.016	0.1
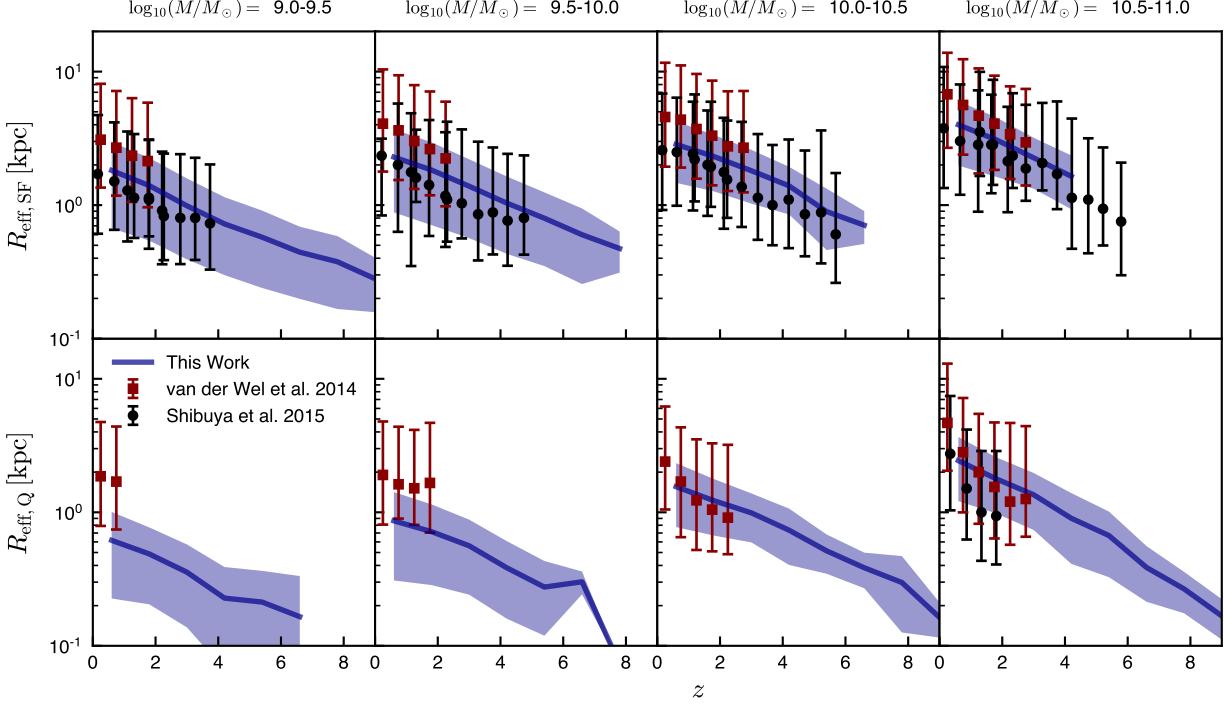
where R_{vir} is the radius of the halo in physical units. We assign R_{eff} values from this mean relation, with log-normal scatter, σ_R. We use the coefficients A and scatter σ_R from Zanisi et al. (2020), as summarized in Table 1. Zanisi et al. (2020) used size distributions of central galaxies from the Sloan Digital Sky Survey (SDSS) DR7 sample (Abazajian et al. 2009; Meert et al. 2016). While these coefficients capture the dependence of R_{eff} on mass and on whether a galaxy is star-forming or quiescent, they are calibrated for $z = 0$ galaxies.

To test whether this relation extends reasonably to higher redshifts, we compare the median $R_{\mathrm{eff}} - z$ relation from our catalog to data from van der Wel et al. (2014) and Shibuya et al. (2015), as shown in Fig. 8. The datasets shown in Fig. 8 consist of galaxies from the 3D-*HST*+CANDELS catalog. Redshifts and masses are from Skelton et al. (2014), and galaxies are classified as either star-forming or quiescent using UVJ diagram criteria.

Fig. 8 demonstrates that our simple assumption that Equation (14) holds for all redshifts agrees remarkably well with the data. We capture the decrease in R_{eff} with both decreasing mass and increasing redshift. We also capture the effect that QGs are smaller than SFGs on average. Our ability to capture redshift trends, despite only using known relations between R_{eff} and R_{vir} at $z = 0$, likely reflects the fact that virial radii evolve as $R_{\mathrm{vir}} \propto 1/(1+z)$, and therefore higher redshift galaxies have smaller virial radii. Our finding that the redshift evolution in the mass-size relation can be captured through the redshift evolution R_{vir} has also been found by Mowla et al. (2019), who show that the ratio r_{80}/R_{vir} is constant for redshifts $z < 3$.

5.2. Axis ratios, Sérsic indices and Position Angles

The distribution of galaxy axis ratios and Sérsic indices should differ between SFGs and QGs (e.g. Franx et al. 2008; Bell et al. 2012; Mortlock et al. 2013) and with redshift (e.g. van der Wel et al. 2011; Guo et al. 2015). To assign shape (defined as the projected axis ratio $q = b/a$, where a is the semi-major half-light size and

Figure 8. Median half-light semi-major radius, $R_{\rm eff}$ as a function of redshift from the synthetic galaxy catalog for SFGs (top) and QGs (bottom). Different columns show different mass bins. The shaded regions are the $1 - \sigma$ standard deviation in each bin for the synthetic galaxies. The points show median data $R_{\rm eff}$ from van der Wel et al. (2014); Shibuya et al. (2015), with the 16th and 84th percentiles of the data point distribution. Our synthetic galaxies match observed trends of galaxy sizes with mass, redshift, and galaxy classification.

b is the semi-minor half-light size) and Sérsic indices, n_s, we use the method directly from Williams et al. (2018). Specifically, using data compiled from van der Wel et al. (2012) and Skelton et al. (2014), Williams et al. (2018) finds the distribution of q and n_s as a function fo redshift. Due to limited data, morphologies for QGs with $z > 4$ are drawn from the $3 \le z \le 4$ distribution, and morphologies for SFGs with $z > 6$ are drawn from the $5 \le z \le 6$ distributions. We use these resulting distributions to draw q and n_s values to assign to each galaxy.

We assign PAs uniformly between 0 and 2π. Synthetic galaxy catalogs often assume that galaxies are oriented isotropically (e.g. Williams et al. 2018), and this assumption will not affect the galaxy clustering, number counts, or cosmic star formation history of our synthetic catalog.

6. GALAXY SEDS

In this section we outline the methods we use to generate galaxy SEDs. The SED pipeline aims to reproduce observed star formation histories and UVLFs, as these quantities dictate the number of ionizing photons produced by galaxies (see Section 7). The SEDs also have realistic SFG and QG properties, including their observed colors, ages, and metallicity (see Appendix B).

6.1. *Overview*

One of the main observables included in the synthetic catalog is the photometry in the *Roman* filters, which requires accurate modeling of the galaxy SEDs. We model the SEDs for each galaxy using the software FSPS (Conroy et al. 2009; Conroy & Gunn 2010). This section serves as an overview of the model used to generate the galaxy SEDs.

We use a Chabrier (2003) initial mass function (IMF), and include the IGM absorption model from Madau (1995). The star-formation history model is described in Section 6.2.1. Additionally, for SFGs, we include the FSPS nebular emission model (Byler et al. 2017) which is controlled by the gas ionization parameter and the gas metallicity. As in Williams et al. (2018), we approximate the stellar and ISM metallicities as a single metallicity value, $Z_{\rm met}$.

The dust modeling includes dust emission and dust absorption. Dust emission follows Draine & Li (2007), which is a silicate-graphite-PAH grain model. The general FSPS dust absorption model follows the commonly used Charlot & Fall (2000) model. We use the Calzetti et al. (2000) attenuation curve, where dust attenuation

is applied to all starlight equally, and therefore depends on one parameter, the total attenuation optical depth $\bar{\tau}_v$. We also include the asymptotic giant branch (AGB) circumstellar dust models from Villaume et al. (2015). Including circumstellar dust can make a significant contribution to the IR emission from galaxies with little diffuse gas, and will need to be included in stellar modeling to accurately interpret data from upcoming IR facilities, including *JWST*.

Overall, this leaves seven free parameters to describe the galaxy SEDs:
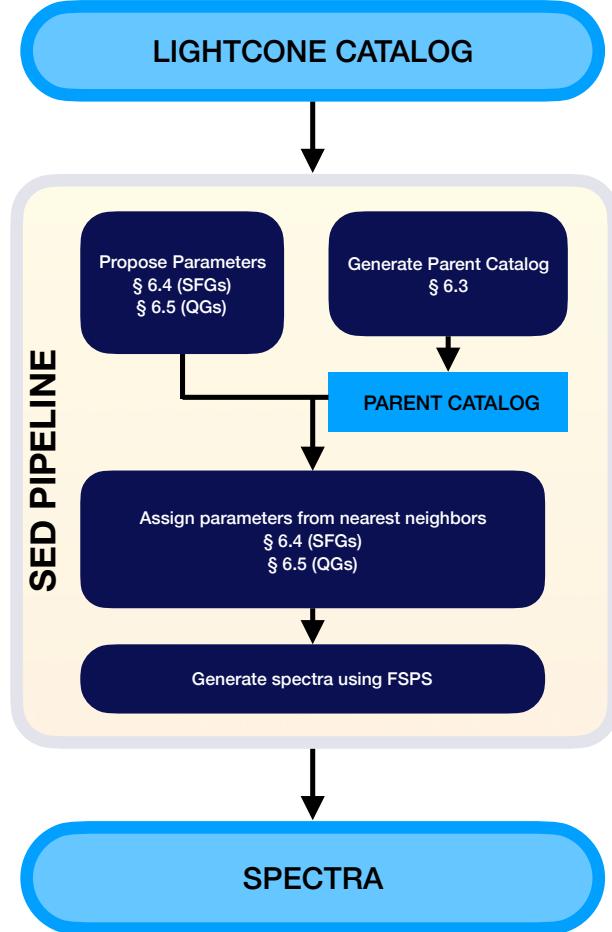
- $M_{\rm gal}$: the stellar mass of the galaxy.

- z: the redshift of the galaxy (or alternatively, $t_{\rm age}$, the age of the universe at that redshift).

- $Z_{\rm met}$: the galaxy metallicity. The gas-phase and stellar metallicities are assumed to be equal.

- $t_{\rm start}$: the age of the universe at the start of star formation.

- τ: the e-folding time for star-formation.

- $\bar{\tau}_v$: the dust attenuation parameter, defined as the opacity at $5500\mathring{A}$.

- U_S: the gas ionization parameter.

In addition to these seven parameters, other relevant quantities included in the synthetic catalog include the star-formation rate (SFR), the UV magnitude, $M_{\rm UV}$, the slope of the UV continuum, β, and the rest-frame colors of the galaxies. Section 6.2 describes the calculation of each of these quantities.

Each galaxy begins with a redshift z (from the lightcone pipeline), a mass, $M_{\rm gal}$ (from abundance matching), and is labeled as either a SFG or a QG, as sampled from the SMF (see Section 3.2). Sections 6.4 and 6.5 below describe SED pipeline for assigning the remaining FSPS parameters ($Z_{\rm met}$, $t_{\rm start}$, τ, $\bar{\tau}_v$ and U_S) for SFGs and QGs, respectively. The pipeline is summarized in Fig. 9.

In brief, we first generate "parent catalogs" for both SFGs and QGs, spanning a realistic range of parameters. These parent catalogs serve as a lookup table for realistic galaxy SEDs. Details on how the parent catalogs are calculated are given in Section 6.3. We propose parameters for each galaxy, and find the 10 nearest neighbors in the parent catalog for each set of galaxy parameters using k-d trees[5]. For SFGs, the proposed parameters are

---

[5] k-d trees are k-dimensional data structures arranged as a binary tree. This structure allows for rapid searches to find the nearest neighbors of a given point in the k-dimensional space.

Figure 9. Overview of the SED pipeline. We begin with a galaxy catalog consisting of redshift and masses for each galaxy, and parent catalogs for the SFGs and QGs. We propose parameters for every galaxy in the catalog and find the nearest neighbors in the parent catalogs. We then assign FSPS parameters based on a weighted average of the nearest neighbors.

$M_{\rm gal}$, z, $M_{\rm UV}$ and β while for QGs, the proposed parameters are $M_{\rm gal}$ and z. The distance metrics used to find the nearest neighbours are detailed in Sections 6.4 and 6.5.

We assign the five free FSPS parameters ($Z_{\rm met}$, $t_{\rm start}$, τ, $\bar{\tau}_v$ and U_S) to each galaxy by taking the weighted average of the nearest neighbors. Given these five parameters, along with the mass and redshift of the galaxy, we use FSPS to generate an SED. We then calculate the UV properties, SFRs and rest-frame colors directly from the spectrum. These calculated properties will not be identical to the proposed parameters, however we still retain the imposed scaling relations in the parent catalogs (see Appendix B).

6.2. *Calculated quantities*

For the SED pipeline outlined above, we need to accurately measure the SFR, rest-frame colors, and UV properties of the galaxy SEDs. This section details the methods we use to measure these quantities. Since FSPS normalizes the stellar modeling, such that one stellar mass is created over the formation history, we scale all the spectra. Specifically, we scale all fluxes and the SFR by M_{gal}/f, where f is the surviving mass fraction in the stellar population, not including stellar remnants.

6.2.1. *Star formation history*

Galaxy SFRs dictate the cosmic star formation rate density (CSFRD) of the universe, which in turn constrains the amount of ionizing photons produced by galaxies in the EoR. Given the importance of SFRs to galaxy evolution and the sources of ionizing photons during the EoR, we need to ensure our synthetic galaxies have SFRs consistent with observations.

The SFR depends on the age, e-folding time and mass of the galaxy. We model the star formation history, $\psi(t)$, using a "delayed tau model", in which:

$$\psi(t) \propto t \exp{-t/\tau} \ , \tag{15}$$

where t is the time since the start of star formation, t_{start}. As discussed in Williams et al. (2018), this parameterization achieves the expectation from simulations that high-redshift galaxies have rising star formation histories (Finlator et al. 2011), and accurately reproduces the colors and mass-to-light ratios of galaxies in smoothed particle hydrodynamics (SPH) simulations (e.g. Simha et al. 2014).

To determine the SFR for each galaxy, we use the FSPS calculated SFR, and scale it by M_{gal}/f, as described above.

6.2.2. *Rest-frame colors*

UVJ diagram galaxy classifications allow for the separation of QGs and dusty SFGs (e.g. Williams et al. 2009; Whitaker et al. 2013; Papovich et al. 2018). To examine the distribution of the synthetic galaxies in UVJ space, we use calculated U-V and V-J colors. Specifically, we use the Johnson U and V filters, and the WFC3 F125W J filter included in FSPS.

6.2.3. *UV properties*

Roman will constrain the number of ionizing photons that are produced by galaxies in the EOR by precisely measuring the UVLF at high redshift. The UVLF depends on the SMF and the UV magnitude, M_{UV} (see Equation 2).

Following Robertson et al. (2013) we define the UV magnitude, M_{UV}, as the average magnitude at rest-frame wavelength in a flat filter, in the range 1450-1550Å. We measure M_{UV} directly from the rest-frame galaxy SEDs by calculating the average flux density:

$$\langle f_\lambda \rangle = \frac{\int_{\lambda_1}^{\lambda_2} f_\lambda d\lambda}{\lambda_2 - \lambda_1} \ , \tag{16}$$

with $\lambda_1 = 1450$Å and $\lambda_2 = 1550$Å.

In addition to the UV magnitude, the slope of the UV continuum, β, helps determine the role of galaxies in ionizing the universe. The slope β is defined as $f_\lambda \propto \lambda^\beta$ (e.g. Meurer et al. 1999). The presence of very blue UV continuum slopes in Roman imaging may provide a signpost of very high escape fractions in early galaxies. We use the method from Dunlop et al. (2012) to determine β. Specifically, we take the SEDs shifted to redshift $z = 7$, and calculate

$$\beta = 4.43(J125 - H160) - 2 \tag{17}$$

using the FSPS included filters F125W and F160W for the Wide Field Camera 3 (WFC3).

6.3. *Parent Catalogs*

We create the parent catalogs by sampling from known scaling relations. By only populating regions of parameter space corresponding to the desired galaxy population, we can fully sample the relevant space, while also limiting the size of the parent catalog. The distributions we use to construct the parent catalogs are summarized in Tables 2 and 3 for SFGs and QGs, respectively, and outlined in detail in this section.

6.3.1. *Star-forming galaxy parent catalog*

For the SFG parent catalog, we sample the seven FSPS parameters for 10^6 galaxies. The mass, redshift, and SFH parameters t_{start} and τ are sampled from uniform distributions, as summarized in Table 2. We sample the dust parameter, $\bar{\tau}_V$ uniformly from a normal distribution centered on zero with a standard deviation of 0.5, truncated between 0 and 4.

Since the metallicity of galaxies depends on the metal production from stars, SFR is related to metallicity. More massive galaxies have higher metallicities on average (the mass-metallicity relation; e.g Lequeux et al. 1979; Tremonti et al. 2004), and the scatter in this relation depends strongly on SFR. The relation between $M_{gal}-Z_{met}-\psi$ is known as the fundamental metallicity relation (FMR; e.g. Mannucci et al. 2010; Hunt et al. 2016), and does not display any significant redshift evolution up to at least redshift $z > 3$ (e.g. Cresci et al.

Table 2. Parameters for SEDs of SFGs. The synthetic galaxies have a fixed parameters $M_{\rm gal}$ and z and "proposed" parameters $M_{\rm UV}$ and β. We identify the 10 closest neighbours in the parent catalog (defined by the distance metric), and assign the final catalog properties $Z_{\rm met}$, U_S, $\bar{\tau}_V$, $t_{\rm start}$ and τ from the nearest neighbors.

Parameter	Proposed Parameter	Parent Catalog	Distance Metric	Assigned Parameter
$M_{\rm gal}$	fixed	uniform in $\log_{10}(M_{\rm gal}/M_\odot) \in [5,12]$	$\log_{10}(M_{\rm gal}/10M_\odot)$	fixed
z	fixed	uniform in $a = 1/(1+z) \in [0.07,1]$	$a = 10/(1+z)$	fixed
$Z_{\rm met}$	...	FMR	...	nearest neighbors
U_S	...	U_S–$Z_{\rm met}$ relation	...	nearest neighbors
$\bar{\tau}_V$	...	$\mathcal{N}(\mu = 0, \sigma = 0.5) \in [0,4]$	...	nearest neighbors
$t_{\rm start}$	...	uniform in $[1\,{\rm Myr}, t_{\rm age}]$	...	nearest neighbors
τ	...	uniform in $[0.1, 100]$ Gyr	...	nearest neighbors
ψ	...	calculated; cut $\log_{10}(\psi/M_\odot {\rm yr}^{-1}) \in [-5,4]$	...	calculated
$M_{\rm UV}$	$M_{\rm UV}$–$M_{\rm gal}$	calculated; cut in $[-25,-5]$	$M_{\rm UV} + 20$	calculated
β	β–$M_{\rm UV}$	calculated; cut in $[-3,-1]$	β	calculated
U-V	...	calculated	...	calculated
V-J	...	calculated	...	calculated

Table 3. Parameters for SEDs of QGs. The synthetic galaxies have a fixed parameters $M_{\rm gal}$ and z. We identify the 10 closest neighbours in the parent catalog (defined by the distance metric), and assign the final catalog properties $Z_{\rm met}$, $\bar{\tau}_V$, $t_{\rm start}$ and τ from the nearest neighbors.

Parameter	Proposed Parameter	Parent Catalog	Distance Metric	Assigned Parameter
$M_{\rm gal}$	fixed	uniform in $\log_{10}(M_{\rm gal}/M_\odot) \in [5,12]$	$\log_{10}(M_{\rm gal}/10M_\odot)$	fixed
z	fixed	uniform in $[0,13]$	$a = 10/(1+z)$	fixed
$Z_{\rm met}$	...	FMR	...	nearest neighbors
$\bar{\tau}_V$	...	$\mathcal{N}(\mu = 0, \sigma = 0.5) \in [0,4]$	...	nearest neighbors
$t_{\rm start}$	...	uniform in $[1\,{\rm Myr}, t_{\rm age}]$	...	nearest neighbors
τ	...	uniform in $[0.01, 10]$ Gyr	...	nearest neighbors
ψ	...	calculated; cut $\log_{10}(\psi/M_\odot {\rm yr}^{-1}) \in [-4,1]$	...	calculated
U-V	...	calculated; cut in UVJ diagram	...	calculated
V-J	...	calculated; cut in UVJ diagram	...	calculated

2019, and references therein). Given these observed trends, we first assign realistic SFRs for galaxies, before assigning metallicities from the FMR.

To assign realistic SFRs, we use the parameterization from Schreiber et al. (2017), constructed to match observations in the redshift range $0 < z < 7$. For SFGs,

$$\log_{10}[\psi/(M_\odot {\rm yr}^{-1})] =$$
$$\log_{10}(M_{\rm gal}/M_\odot) - 9.5 + 1.5\log_{10}(1+z)$$
$$0.3[\max(0, \log_{10}(M_{\rm gal}/M_\odot) - 9.36 - 2.5\log_{10}(1+z))]^2 \quad (18)$$

with a log-normal scatter of 0.3 dex.

We then propose $Z_{\rm met}$ by drawing from the FMR presented in Williams et al. (2018) (based off of data from

Hunt et al. 2016)

$$\log_{10}(Z_{\rm met}/Z_\odot) + 8.7 \approx 12 + \log_{10}({\rm O/H})$$
$$= -0.14\log +10(\psi/M_\odot {\rm yr}^{-1}) \quad (19)$$
$$+0.37\log_{10}(M_{\rm gal}/M_\odot) + 4.82$$

with scatter from a Student's t-distribution with 3 degrees of freedom, a standard deviation of 0.3 in $\log_{10}(Z_{\rm met}/Z_\odot)$, and truncated between $-2.2 < Z_{\rm met} < 0.24$. A Student's t-distribution is more heavily tailed than a Gaussian, and agrees better with observational data. As discussed in Williams et al. (2018), imposing a maximum metallicity, $\log_{10}(Z_{\rm met}/Z_\odot) = 0.24$, in the synthetic galaxies reproduces the observed turnover in the mass–metallicity relation, despite the fact that Equation 19 is linear in mass. We use the same FMR to assign metallicities to both SFGs and QGs, as we find that existing measurements of quiescent galaxies are

consistent with the FMR used to create this synthetic catalog (e.g Peng et al. 2015; Leethochawalit et al. 2018).

Gas-phase metallicity is also an indirect tracer of gas flows in galaxies. Metallicity and stellar mass both correlate with star formation history, but gas flows will introduce scatter in the metallicity and stellar mass relation. Thus, the gas ionization parameter, U_S (which represents the ratio of the number density of ionizing photons to the number density of hydrogen atoms) correlates with metallicity. To assign the gas ionization parameter, we use the low-redshift relation from Carton et al. (2017):

$$\log_{10} U_S = -0.8 \log_{10}(Z_{\mathrm{met}}/Z_\odot) - 3.58 \qquad (20)$$

with a scatter of 0.3 dex sampled from a Student's t-distribution with three degrees of freedom, truncated between $-4 < \log_{10} U_S < -1$. As in Williams et al. (2018), we assume the relation holds at all redshifts.

Given the seven FSPS parameters, we then calculate M_{UV}, β, ψ as outlined in Section 6.2. We discard galaxies that have unrealistic ψ, M_{UV} or β values, as summarized in Table 2. The resulting SFG parent catalog has $\sim 9 \times 10^5$ galaxies.

6.3.2. Quiescent galaxy parent catalog

We generate the parent catalog for the QGs in a similar way to the parent catalog for the SFGs. For 10^7 galaxies, we assign galaxy masss, redshifts, and SFH parameters t_{start} and τ from uniform distributions, as summarized in Table 3. We sample the dust parameter, $\bar{\tau}_V$ uniformly from a normal distribution centered on zero with a standard deviation of 0.5, truncated between 0 and 4.

We assume QG metallicities, Z_{met}, follow the same FMR as SFGs, as given in Equation 19, which is consistent with existing measurements of quiescent galaxies (e.g Peng et al. 2015; Leethochawalit et al. 2018). We propose SFRs from Schreiber et al. (2017) as before. For quiescent galaxies,

$$\log_{10}[\psi/(M_\odot \mathrm{yr}^{-1})] = 0.5 \log_{10}(M/M_\odot) + \log_{10}(1+z) - 6.1 \;, \qquad (21)$$

with a log-normal scatter of 0.45 dex.

As before, given the seven FSPS parameters, we then calculate ψ and the UVJ colors, as outlined in Section 6.2. We remove any galaxies in the QG parent catalog that do not fall in the proper space in the UVJ diagram, to avoid including any galaxies with unrealistic colors. Specifically, we use the criteria that a galaxy can be classified as SF if it satisfies any of the following

conditions

$$U - V < 1.3$$
$$V - J > 1.6 \qquad (22)$$
$$U - V < 0.88(V - J) + 0.49$$

(Williams et al. 2009). After cuts in SFR and UVJ, the resulting parent catalog has 5×10^4 galaxies. Though SFR not set explicitly for QGs, these cuts ensure that QGs have a low SFR, differentiating them from the SFG population (see Appendix B).

6.4. Star-forming galaxies

This section outlines our procedure for assigning realistic SEDs for SFGs. To accurately capture the observed CSFRD and UVLFs, galaxies must have realistic SFRs and UV magnitudes. We also aim to produce realistic UV continuum slopes, β, the fundamental mass relation (FMR), and the relationship between metallicity and gas ionization. Overall, we propose five parameters to define the SFG SEDs, ψ, M_{UV}, β, Z_{met}, and U_S. Details of how these proposed parameters are generated, and how the FSPS parameters are determined for the SFGs are given in this section, and summarized in Table 2.

To reproduce observed UVLFs, the synthetic galaxies need to follow the same $\bar{M}_{\mathrm{UV}} - M_{\mathrm{gal}}$ relation that Williams et al. (2018) used to generate the high-redshift SMFs used in this work:

$$\bar{M}_{\mathrm{UV}} = -1.66(M_{\mathrm{gal}} - b_{M_{\mathrm{UV}}}) - 20$$

$$b_{M_{\mathrm{UV}}} = \begin{cases} 0.12z^2 - 0.98z + 11.4175 & \text{for } z \le 3.75 \\ -0.12z + 9.88 & \text{for } 3.75 < z < 8 \\ 8.92 & \text{for } z \ge 8 \end{cases}$$
$$(23)$$

Additionally, Williams et al. (2018) found that scatter observed in 3D-HST data (Skelton et al. 2014) is constant in both stellar mass and redshift, with an average value of $\sigma_{\mathrm{UV}} = 0.7$. Therefore, we propose M_{UV} values from Equation (23) with a Gaussian scatter of $\sigma_{\mathrm{UV}} = 0.7$.

We also use the relations from Williams et al. (2018) to propose UV continuum slopes, β,

$$\beta = m_\beta(M_{\mathrm{UV}} + 19.5) + b_\beta$$

$$b_\beta = \begin{cases} -0.09z - 1.49 & \text{for } z \le 8 \\ -0.77 & \text{for } z > 8 \end{cases} \qquad (24)$$

$$m_\beta = \begin{cases} -0.007z - 0.09 & \text{for } z \le 8 \\ -0.146 & \text{for } z > 8 \;. \end{cases}$$

Given the proposed galaxy properties, we next determine which FSPS parameters to assign. To generate

SEDs that match closely to the proposed parameters, we find the 10 nearest neighbors the SFG parent catalog. Table 2 outlines the distance metric we use to find the nearest neighbors. We average the five free FSPS parameters ($Z_{\rm met}$, $t_{\rm start}$, τ, $\bar{\tau}_v$ and U_S) of these neighbors, with a weight based on their distance to the proposed parameters. In cases where the assigned $t_{\rm start}$ value is greater than $t_{\rm age}$, we set $t_{\rm start} = t_{\rm age}$. This method allows us to "fit" the target (proposed) parameters, even with the very large number of galaxies, something that would not be computationally realistic to achieve iteratively.

Given the large degeneracies between different galaxy properties (e.g. age, metallicity, dust, star formation history) we find that our solution depends sensitively on how realistically we populate the parent catalogs, and also how we define the distance metric. In particular, we find that to ensure the final parameters were close to the proposed parameters, it is especially important to find neighbors that are close in redshift.
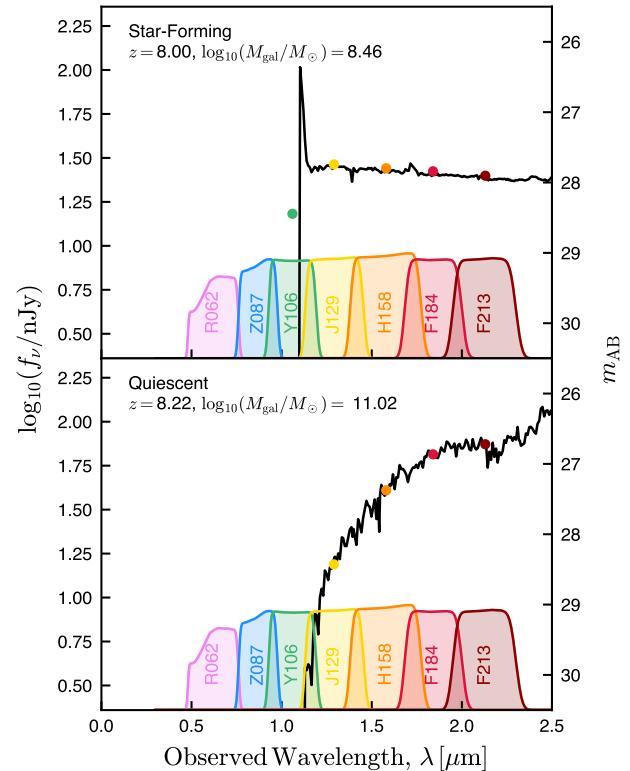
6.5. Quiescent galaxies

In addition to SFGs, we include a QG population. We turn off the nebular emission model for QGs, as low redshift galaxies are known to have very low gas content. Though galaxy modeling often assumes QGs do not contain any gas or dust (e.g. Williams et al. 2018), recent results from Gobat et al. (2018) suggest that higher redshift galaxies should have significant dust content. We therefore include dust for the QGs. We assign QG properties in a similar we assign SFG properties. Given the QG parent catalog described in Section 6.3, we determine FSPS parameters using the 10 nearest neighbors in mass and redshift. We summarize the details of this procedure in Table 3.

6.6. Example SEDs

We present the resulting SEDs for two example galaxies at redshift $z \sim 8$ in Fig. 10. The *Roman* WFI filters include seven photometric filters: R062, Z087, Y106, J129, H158, F184, F213[6], a wide-field filter W146, a grism, and a prism. We plot the flux calculated in the seven photometric filters R062, Z087, Y106, J129, H158, F184, and F213. Both galaxies show a clear Lyman break in Y106.

The SFG (top panel) should be selected as a Lyman break galaxy (LBG) in *Roman* using the common Lyman-break method. This example also displays

Figure 10. Example SEDs for a SFG (top) and a QG (bottom) at redshift $z \approx 8$. The Roman photometric filters (R062, Z087, Y106, J129, H158, F184, and F213) are overplotted. The observed magnitudes in each band are shown as colored points. The SFG would be selected in this UDF as a LBG using *Roman* photometry.

strong Ly-α emission. Ly-α emitters (LAEs) are a common way to study study the EoR, and *Roman* will detect many such galaxies. Quantifying the science returns of LAEs in a *Roman* UDF will be the subject of future work.

Due to the SMFs we used to construct our catalog, we model a small population of high-redshift QGs, such as the one shown in the bottom panel of Fig. 10. It is unclear whether redshift $z = 8$ galaxies exist, or what the mechanism of their formation would be. Due to the large area a deep survey with *Roman* will cover, a *Roman* UDF could help identify rare high-redshift quiescent galaxies if they exist. This will be discussed further in Section 9.2.

7. COSMIC STAR FORMATION HISTORY

Since one of the main goals of a *Roman* UDF is to study the ionizing photon contribution from galaxies, we ensure we reproduce observed UVLFs (Section 7.1) and the CSFRD (Section 7.2). Additional galaxy properties are discussed in Appendix B to show the range

---

[6] The F213 was recently added; the science justifications for this filter are outlined in Stauffer et al. (2018). The higher background in F213 will result in brighter flux limits compared to bluer Roman bands.

of scientific questions our synthetic galaxy catalog can address.
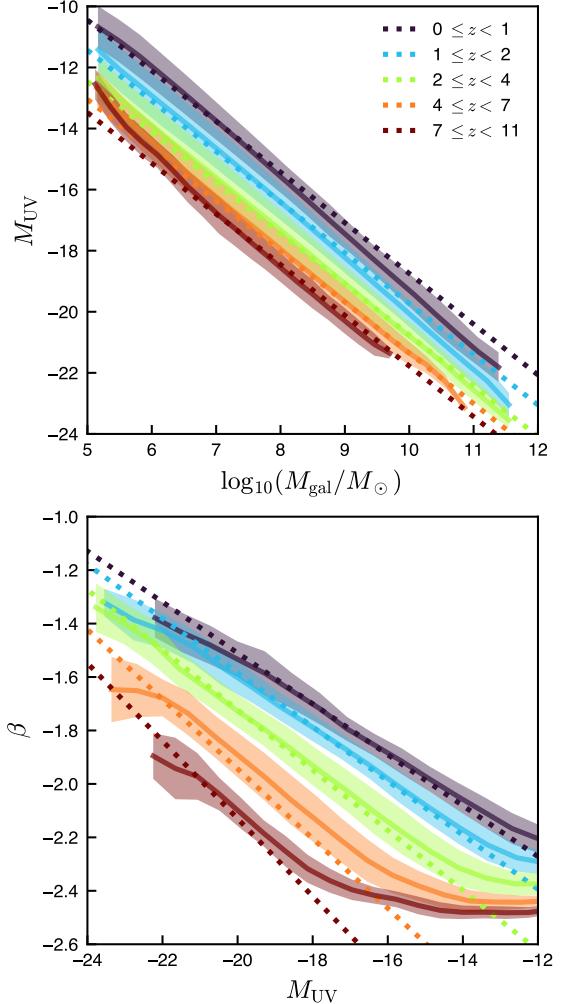
7.1. UV properties

Placing strong constraints on the faint end of the UVLF during the EoR is a main goal of a *Roman* UDF. To reproduce observed UVLFs, the synthetic galaxies must follow the correct distribution of $M_{\rm UV}$, as discussed in Section 6.2.3. On average, the UV magnitude, $M_{\rm UV}$, decreases (becomes brighter) with galaxy mass, $M_{\rm gal}$ (e.g. Stark et al. 2009). For galaxies with $\log_{10}(M_{\rm gal}/M_\odot) > 10$ the relationship flattens (e.g. Spitler et al. 2014). Apart from this flattening at high masses, the observed $M_{\rm UV}$–$M_{\rm gal}$ relation has a constant slope, with the normalization evolving with redshift (e.g. Duncan et al. 2014; Stefanon et al. 2017). Similarly, the UV continuum slope, β, correlates with $M_{\rm UV}$. Though the exact relation between β and $M_{\rm UV}$ is still studied, β appears bluer (decreases) with increasing (fainter) $M_{\rm UV}$ and increasing redshift (e.g. Bouwens et al. 2014).

We calculate the UV properties, $M_{\rm UV}$ and β, of the synthetic SFGs as described in Section 6.2.3, and presented in Fig. 11. We reproduce trends for both $M_{\rm UV}$ and β imposed from Williams et al. (2018). The $M_{\rm UV}$-mass relation enables us to reproduce observed UVLFs, as discussed below. We also closely reproduce the β–$M_{\rm UV}$ relation for $\beta > -2.5$. Below $\beta < -2.5$, our galaxy catalog agrees with studies that indicate that the β–$M_{\rm UV}$ relationship flattens for $M_{\rm UV} \gtrsim -19$ galaxies (e.g. Bouwens et al. 2014).
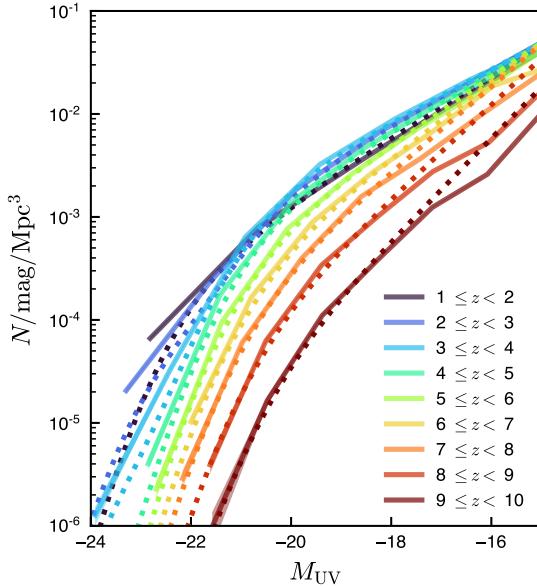
We show the UVLFs of our synthetic SFGs in Fig. 12, compared to the UVLFs that are expected from convolving the SMF with a normal distribution, centred on $M_{\rm UV}$ (Equation 2). The galaxy catalog agrees very well with the imposed relation, and is consistent with current observations, as shown in Section 8.3. Our catalog has slightly less galaxies at faint magnitudes ($M_{\rm UV} > -17$) than expected due to the fact that we do not perfectly recreate the $M_{\rm UV}$–$M_{\rm gal}$ relationship. These magnitudes are fainter than the detection limits of a $30\,m_{\rm AB}$ survey, and our synthetic catalog UVLF is consistent with current observations, as discussed in Section 8.3.

7.2. Cosmic star formation rate density

As discussed in Section 6.2.1, the CSFRD describes the ionizing photon contribution of galaxies as a function of cosmic time (for a review, see e.g. Madau & Dickinson 2014). We display the evolution of the CSFRD in the top panel of Fig. 13. We calculate the CSFRD by taking the sum of galaxy SFRs, ψ (averaged over the last 100 Myr), in each bin divided by the comoving volume of the bin. As in Williams et al. (2018), to compare to Madau

Figure 11. Average $M_{\rm UV}$–mass relation (top) and β–$M_{\rm UV}$ relation (bottom) for SFGs in the synthetic catalog (solid lines) and the standard deviation in the bin (shaded region). We compare the synthetic catalog to the relations from Williams et al. (2018), calculated as the volume-weighted average over the redshift bin (dotted lines). The synthetic galaxy catalogs are constructed to match the underlying $M_{\rm UV}$–mass relations, to reproduce observed UVLFs. The synthetic galaxy catalog matches the underlying relations closely, except for a flattening in the β–$M_{\rm UV}$ relation for faint galaxies. This flattening is consistent with current constraints, as described in Section 7.1.
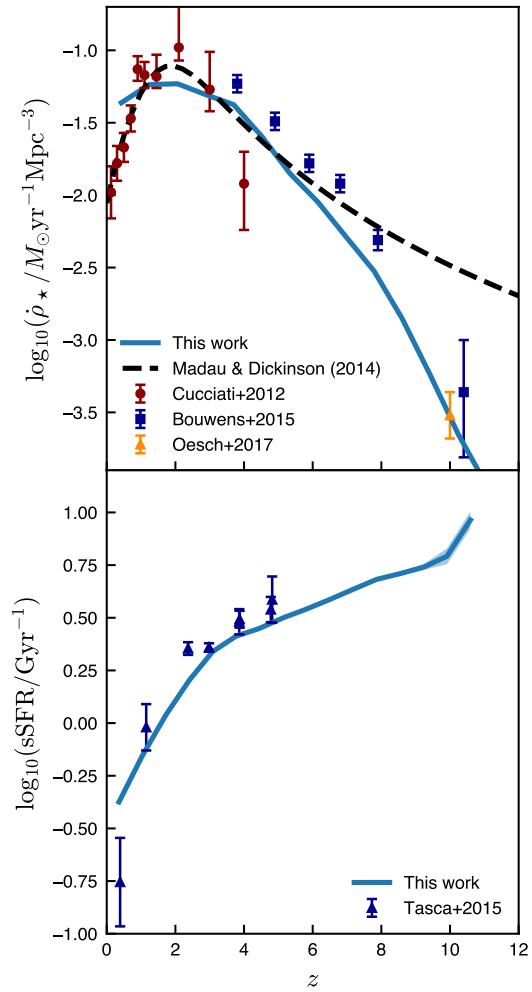
Figure 12. UV luminosity function of the synthetic galaxy catalog. The dotted lines show the expected UVLF from convolving the Williams et al. (2018) SMF with the $M_{\rm UV}$–$M_{\rm gal}$ relationship (Equation 2), and then averaged over the redshift bin. Overall, the data matches the underlying relations very well, and agrees with current observations (see Fig. 18).

& Dickinson (2014), we imposed a luminosity limit of $0.03\,L_*$.[7]

Similar to Williams et al. (2018), we find that the CS-FRD agrees roughly with the model presented in Madau & Dickinson (2014), but more closely to data (e.g. Cucciati et al. 2012; Oesch et al. 2018). Most notably, our synthetic galaxies agree with high-redshift ($z > 8$) measurements of the CSFRD. As in Williams et al. (2018), our synthetic galaxies have a slight deficit at redshifts $1 < z < 3$, which reflect the underlying SMFs. As discussed in Williams et al. (2018), the SMFs we used do not include the dusty SFGs currently missed in the UV-selected samples.

We show the evolution of the specific star formation rate (sSFR) in the bottom panel of Fig. 13, for galaxies with $8.8 < \log_{10}(M_{\rm gal}/M_\odot) < 10$. We calculate the median sSFR by dividing the SFR averaged over the last 100 Myr by the galaxy mass. For comparison, we plot data from Tasca et al. (2015). The synthetic galaxies

[7] The equivalent limit in $M_{\rm UV}$ is $M_{\rm UV} \sim -14.5$ at $z < 1$ (Cucciati et al. 2012), $M_{\rm UV} \sim -15.5$ at $1 < z < 2$ (Cucciati et al. 2012), $M_{\rm UV} \sim -16.89$ at $2 < z < 2.7$ (Reddy & Steidel 2009), and $M_{\rm UV} \sim -17$ at $z > 2.7$ (Bouwens et al. 2015, 2016; Finkelstein et al. 2015; Oesch et al. 2018).

Figure 13. Evolution of star formation in the universe. Top: evolution of the CSFRD of synthetic galaxies with a luminosity limit of $0.03\,L_*$ (dark blue). Error bars are smaller than the width of the line. The dashed black line is the CSFR density of the universe compiled by Madau & Dickinson (2014), and colored points are measurements from the literature (Cucciati et al. 2012; Bouwens et al. 2015; Oesch et al. 2018). The data are converted from a Salpeter (1955) to a Chabrier (2003) IMF by dividing the CSFRD by a factor of 1.7. Bottom: the redshift evolution of the median sSFR of $8.8 < \log_{10}(M_{\rm gal}/M_\odot) < 10$ synthetic galaxies (solid line) compared to measurements from the literature (colored points; Tasca et al. 2015). Overall, the cosmic star formation history of the synthetic galaxy catalogs is in close agreement with observational data.

and observations agree very well. The sSFR of galaxies at redshifts $z > 4$ is a matter of active research, but we find an increase in sSFR, consistent with current studies (Stark 2016). Given that our galaxy catalog is consistent

with observations for both galaxy clustering and cosmic star formation histories, we now turn our attention to making preliminary predictions for the science returns of a *Roman* UDF.
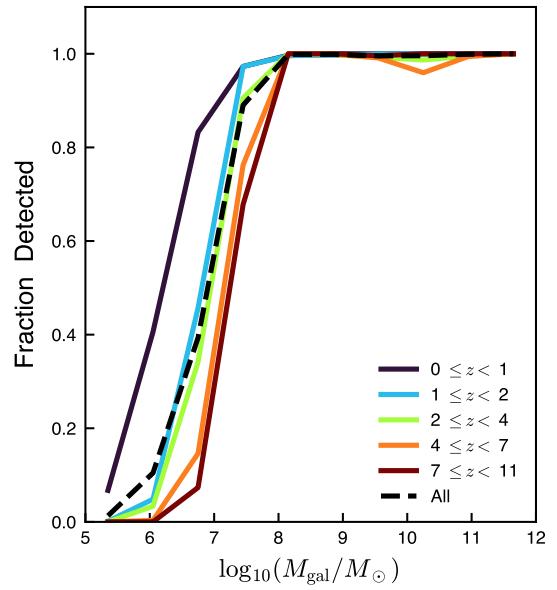
8. PREDICTIONS FOR A ROMAN ULTRA-DEEP FIELD SURVEY

In this section, we demonstrate the capabilities of a 1 deg^2 *Roman* UDF to study the earliest galaxies at the EoR and beyond. We begin by discussing our method for determining whether a galaxy is selected (Section 8.1), and the expected galaxy number counts (Section 8.2), before presenting our projected constraints (Section 8.3). Throughout this section we compare our predictions for a *Roman* UDF to the best current constraints in the literature. However, by the time *Roman* launches *JWST* will have provided an extraordinary amount of data, greatly enhancing our understanding of the universe. We discuss synergies between a *Roman* UDF and *JWST* in Section 9.4.

8.1. *Selection criteria*

Understanding of galaxy formation increased immensely when techniques to select high redshift ($z > 5$) galaxies were developed (for review see, e.g. Dunlop 2013). The most commonly used method is the Lyman-break technique, which selects LBGs based on a step in the blue UV continuum emission at $\lambda_{\rm rest} = 1216$ Å. To determine whether a UDF with *Roman* would select each galaxy in the synthetic catalog, we use a magnitude limit based on the Lyman-break, in the same manner as Williams et al. (2018). Specifically, for each filter, we assign a non-overlapping wavelength range (the dividing point was taken to be halfway between the centres of two adjacent bands). Each galaxy is assigned a "dropout" filter, according to the wavelength that corresponds to its Lyman-break, $\lambda = 1216(1 + z)$Å. If a galaxy is brighter than the magnitude limit in the band immediately redder to its dropout filter, we consider it to be detectable. We use the magnitude limit $m_{\rm AB} = 30$ for a 5σ detection.

We show the fraction of detectable galaxies in Fig. 14. The mass at which $\sim 50\%$ of galaxies ranges from $\sim 10^6$ at $z \approx 1$ to 10^7 at $z = 10$. We find that nearly 100% of galaxies are detectable above masses of $M_{\rm gal} = 10^8 M_\odot$, which indicates that there should be very tight constraints on galaxy properties (such as galaxy clustering and UVLFs) above this mass. Given this, we can measure the clustering of faint galaxies ($M_{\rm UV} \lesssim -18$) at the EoR. With completeness corrections, we can measure quantities such as the UVLFs for galaxies brighter

Figure 14. Fraction of detectable galaxies (5σ) in the Roman synthetic catalog. Nearly all galaxies with masses $M_{\rm gal} > 10^8 M_\odot$ (corresponding to $M_{\rm UV} < -18$) are detectable out to redshifts $z \approx 10$.
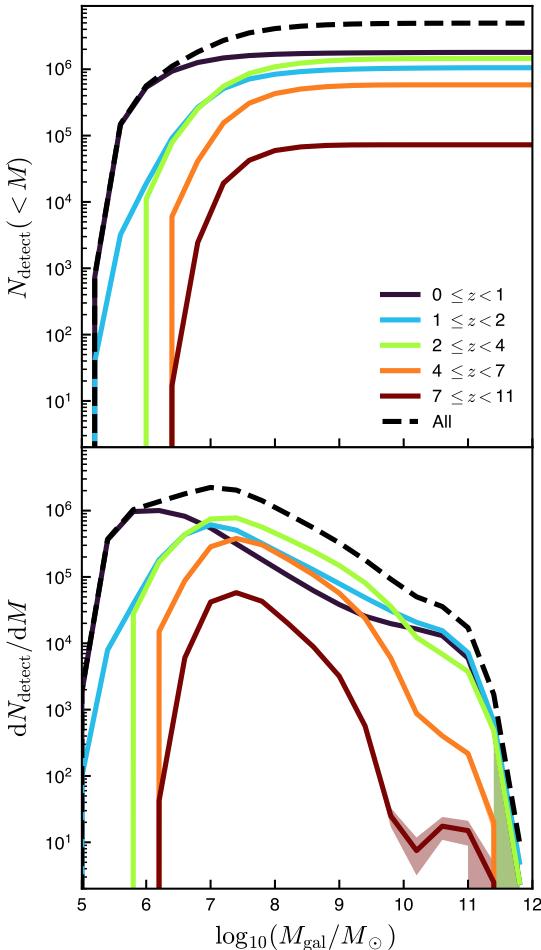
than $M_{\rm UV} \approx -17$ out to redshifts $z \approx 10$. Section 8.3 will explore these potential constraints in more detail.

In the following sections, we assume that any detectable galaxy is selected. This approach assumes that there is no scatter in the photometric redshifts, and no galaxies are obscured by forefront galaxies. Future work will examine *Roman* UDF constraints in more detail, taking into account these effects. The catalogs and images presented in this work will be instrumental to explore these sources of systematic errors.

8.2. *Number counts*

Here we provide number counts of the detectable galaxies (5σ), to understand the science returns of a *Roman* UDF and measure the completeness of the survey. Fig. 15 shows both the cumulative number counts (top), and the differential number counts (bottom). We find that a 1 deg^2 *Roman* UDF could detect more than 10^4 galaxies at redshifts $z > 7$. For comparison, *HST* has detected on the order of 10^3 galaxies at redshifts $z \sim 4$–10 (Koekemoer et al. 2013; Lotz et al. 2017), and Cycle 1 *JWST* programs are expected to detect ~ 5000 galaxies at redshifts $z > 6$ (Williams et al. 2018).
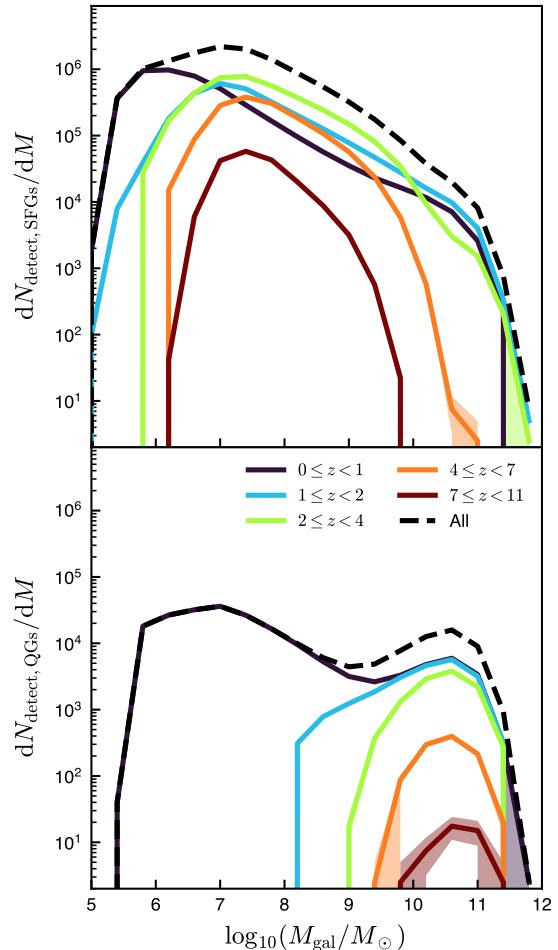
Though a UDF catalog will consist largely of SFGs, there will also be a number of QGs, as demonstrated in Fig. 16. These predictions indicate that a 1 deg^2 will contain a handful of detectable QGs above redshift $z = 7$ if they exist. In combination with e.g. *JWST*

Figure 15. The cumulative (top) and differential (bottom) number counts of the detectable galaxies (5σ) in our *Roman* UDF synthetic catalog. A *Roman* UDF will contain over a million galaxies, with tens of thousands in the EoR.

Figure 16. Number counts of detectable galaxies (5σ) for SFGs (top) and QGs (bottom) in our *Roman* UDF synthetic catalog. A *Roman* UDF will detect QGs out to very high redshifts, possibly even detecting a few at the EoR.

spectroscopy, this could identify $z > 7$ QGs. Given that we currently have only detected QGs out to redshifts of $z \sim 4$–5 (Merlin et al. 2019; Valentino et al. 2020), this will greatly enhance our understanding of the QG population. Determining the number and mass distribution of high-redshift QGs is fundamental to understanding galaxy evolution, and for testing different models for the emergence of QGs (see, e.g. Cortese et al. 2021, for a recent review on quenching).

Due to the nature of these kinds of predictions, the underlying galaxy properties in the catalog are extrapolated beyond our current knowledge (in particular, the number of low-mass objects is dependent on extrapolations of the SMFs). Therefore, the number counts pre-

sented in this section represent a reasonable estimate of what a UDF might see, but there is much to be learned in the future. Regardless, the large number of galaxies that *Roman* will detect will provide the best census to date of faint high-redshift galaxies, including those thought responsible for reionizing the universe.

8.3. *The science returns of a Roman UDF*

Some of the quantities that a *Roman* UDF will aim to constrain include the SMF, the UV luminosity function, galaxy clustering and the galaxy–halo connection at high redshifts. In this section we provide preliminary projected constraints for a $1 \deg^2$ *Roman* UDF, based on the detectable galaxies identified in Section 8.1. We

have not included uncertainties from cosmic variance or from errors on photometric redshifts in our predictions, as that is beyond the scope this paper. However, we note that our synthetic catalog provides the basis for rigorous studies of systematic errors in a *Roman* UDF, and will be the focus of future work.

8.3.1. *Stellar mass functions*
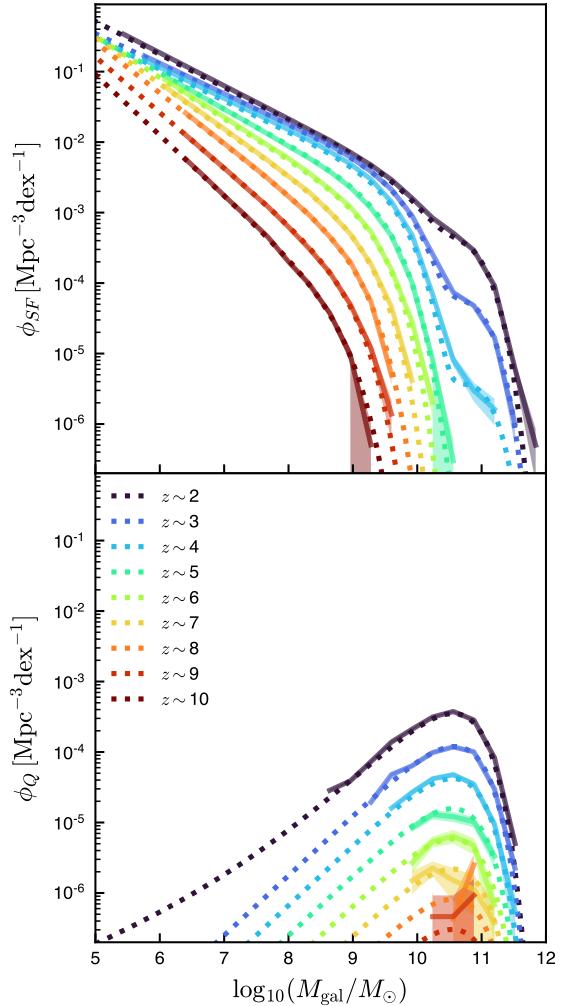
The evolution of the SMF of galaxies over cosmic time provides information on how galaxy populations have evolved, the star-formation history of the universe, and the galaxy–halo connection. Fig. 17 shows the SMF for the detectable galaxies in the synthetic catalog, with the underlying SMFs shown as dotted lines for both SFGs (top) and QGs (bottom). We perform a completeness correction by dividing the number of detectable galaxies by the fraction of detectable galaxies at the corresponding mass and redshift. As shown in Fig. 6, our synthetic catalog matches the SMF nearly exactly by construction.

For our catalog, the SMF for the detectable SFGs is measurable to masses of $M_{\rm gal} > 10^{6.5}\,M_\odot$ for all redshifts. For the detectable QGs, the SMF is measurable to redshifts $z \sim 7$ (masses $M_{\rm gal} > 10^{9.5}\,M_\odot$). In comparison, observations have only recently placed *any* constraints on the SFG SMF at redshift $z = 8$–10. Further, these constraints only exist for galaxies with $M_{\rm gal} < 10^8\,M_\odot$, and have very large uncertainties (about 100%; Stefanon et al. 2021). Measurements of QG SMFs only extend to redshifts $z \approx 4$ (e.g. Girelli et al. 2019).

The exact constraints on a SMF from *Roman* will depend on stellar mass measurements and the accuracy of completeness corrections. This work provides a first calculation of the completeness of a *Roman* UDF (Section 8.1), and highly realistic simulated data to enable future rigorous calculations. In practice, stellar mass estimates of high redshift galaxies will require photometry redshifts beyond the reddest *Roman* filters. However, *JWST* will provide tight constraints on the $M_{\rm UV}$–$M_{\rm gal}$ relation which can be used to estimate stellar masses of galaxies in a *Roman* UDF.

8.3.2. *UV luminosity functions*

To clearly answer whether there were enough galaxies during the EoR to reionize the universe, we need strong constraints on the faint end of the UVLF during the EoR. Bouwens et al. (2021) provide the most recent, comprehensive constraints on the UVLF, and are able to constrain the faint end ($M_{\rm UV} < -17$) out to redshift $z \sim 10$. At redshift $z \sim 10$, only 8 sources are used to constrain the UVLF, so the uncertainties are very large (∼50–100%). In comparison, a *Roman* UDF could

Figure 17. SMF of the detectable galaxies (5σ) in our synthetic galaxy catalog for SFGs (top) and QGs (bottom), with completeness corrections. The synthetic galaxies agree with the Williams et al. (2018) SMFs (dotted lines) by construction. A *Roman* UDF can potentially constrain the SMF beyond redshift $z = 10$ ($M_{\rm gal} > 10^{6.5}\,M_\odot$) for SFGs, and to redshift $z \approx 7$ ($M_{\rm gal} > 10^{9.5}\,M_\odot$) for QGs.

detect ∼ 10^3 sources at $z \sim 10$, and thus greatly reduce the uncertainties in the UVLF.

We show the UVLF of the detectable synthetic galaxies in Fig. 18, compared to the data from Bouwens et al. (2021). As in the previous section, we perform a completeness correction by dividing the number of selected galaxies by the fraction of selected galaxies at the corresponding mass and redshift. We predict a *Roman* UDF will be able to constrain the UVLF beyond redshift $z \approx 10$, with galaxies $M_{\rm UV} < -17$. Due to the vast number of galaxies in a *Roman* UDF, it could constrain

the faint-end UVLF to within ~ 1 percent to redshifts $z \gtrsim 10$, far tighter than existing limits.

We note that the bright end of the synthetic galaxy catalog UVLF is higher than the Bouwens et al. (2021) data at low redshifts. As shown in Fig. 12, our galaxy catalog agrees with the underlying UVLF model we used at the bright end, and therefore this difference can be attributed to the SMFs used in this work. This excess of low-redshift ($z < 4$), bright galaxies is consistent with the possibility of inefficient mass quenching, low dust obscuration, or hidden AGN activity, as suggested by Harikane et al. (2021).

8.3.3. *Galaxy clustering*

Roman's wide, contiguous field of view will allow measurements of the 2PCF of faint galaxies at the time of reionization and thus their underlying dark matter halo masses. To date, halo masses have only been strongly constrained to redshifts $z \sim 6$, and are limited to bright ($M_{\rm UV} \sim -20$) galaxies at redshifts $z = 4$–6 (e.g. Harikane et al. 2018). JWST will potentially provide the first measurement of the clustering of high-redshift galaxies (Endsley et al. 2020), but due to its smaller field of view, it will likely suffer from cosmic variance, and will not have the same capability as *Roman* to study clustering in different environments.

We measure the 2PCF of the detectable galaxies in the $1\,{\rm deg}^2$ survey, as outlined in Section 4.3. We included all galaxies brighter than $M_{\rm UV} < -18$. Fig. 19 shows the measured 2PCF. The 2PCF for these faint galaxies is measured to very high accuracy (within 1%) out to redshifts $z \approx 7$, with constraints out to $z \approx 10$ (to within 10%).

8.3.4. *Galaxy–halo connection*

In addition to constraining the number and spatial distribution of faint, high-redshift galaxies, *Roman* will also provide constraints on the galaxy–halo connection. Galaxy clustering can be used to infer dark matter halo mass, as the underlying dark matter will dictate the gravitational field (Mo & White 1996). Together with galaxy mass measurements, galaxy clustering gives a direct measure of the SHMR (which summarizes the connection between galaxy masses and their host dark matter halos).

As discussed above, halo masses have only been measured directly for redshifts $z \lesssim 6$ (e.g. Harikane et al. 2018), while at high redshifts, SHMR constraints have been achieved with abundance matching between observed stellar masses and dark matter only simulations (e.g. Stefanon et al. 2021). There is a potential disagreement between these two techniques—the SHMR measured from abundance matching is typically 3–4 times

higher than that measured from clustering (Stefanon et al. 2021). The difference between SHMRs derived from clustering and AM indicates that direct halo mass measurements are needed to understand the galaxy–halo connection at high redshifts. A *Roman* UDF will provide extraordinary data, which may elucidate the origin of this discrepancy.

We show the SHMR for our synthetic galaxy catalog in Fig. 20, and recent constraints from Harikane et al. (2018) and Stefanon et al. (2021). The Stefanon et al. (2021) data were scaled down by a factor of 1.7 to convert from a Salpeter (1955) IMF to a Chabrier (2003) IMF. We use all the 5σ Lyman-break selected galaxies in the catalog. Our synthetic catalog clustering measurements agree well with the Stefanon et al. (2021) data (within $\sim 1\sigma$), and are slightly higher than the Harikane et al. (2018) data.

In this work we do not attempt to predict how well a *Roman* UDF will be able to constrain the SHMR. As discussed in Section 8.3.1, stellar mass measurements for high-redshift galaxies likely require photometry at wavelengths longer than what *Roman* will provide, but may be possible to estimate with scaling relations. Since our synthetic galaxy catalogs contain information regarding host dark matter halo properties, this work can form the basis of future analyses of the galaxy–halo connection in UDFs.
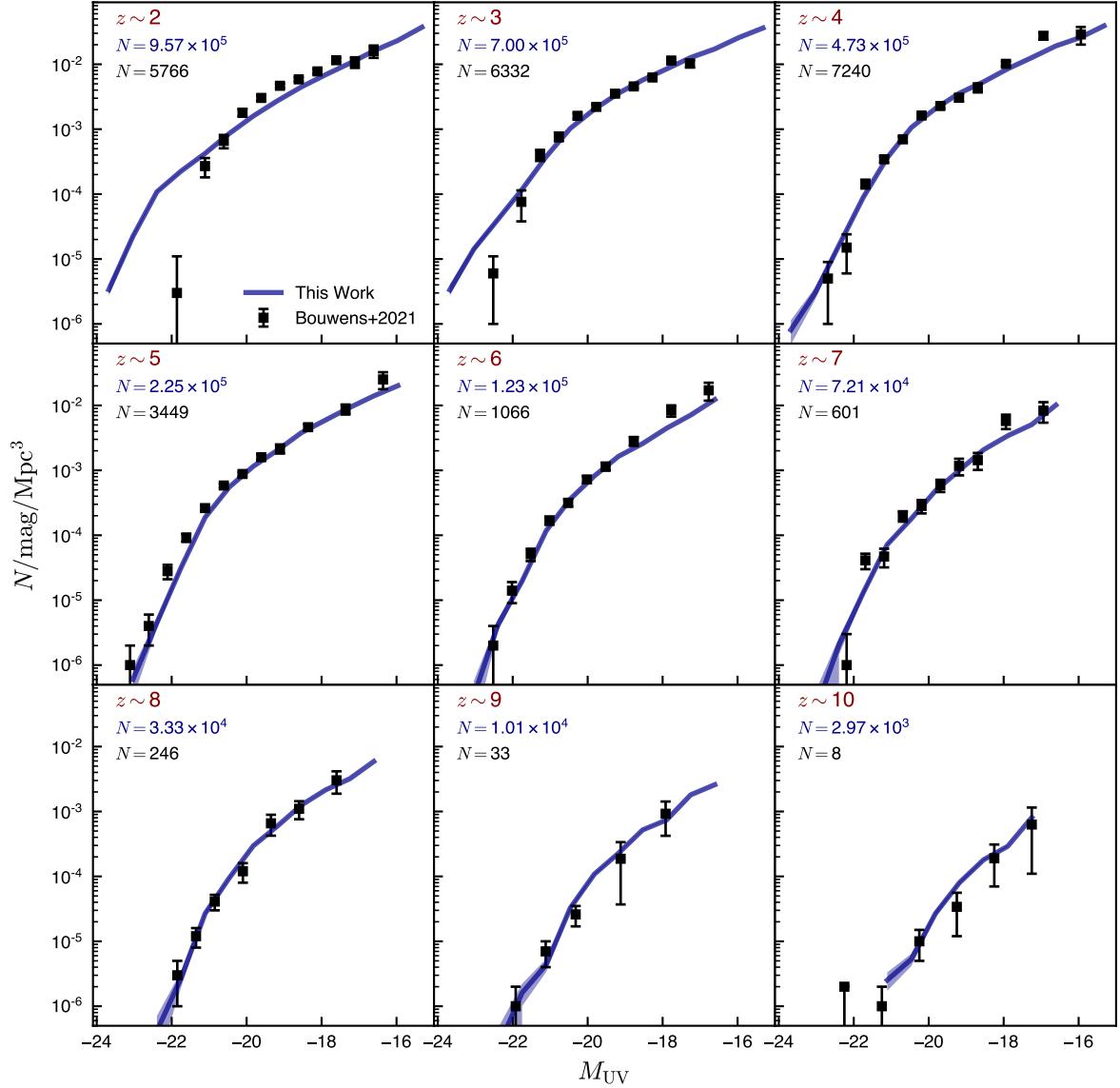
8.4. *Synthetic images*

In addition to the galaxy catalog, we present synthetic images of a *Roman* UDF. These images are intended for developing analysis tools, and studying systematics (see Section 9.5). Full resolution versions of the RGB images presented in this section in our data release (see Appendix A for details).
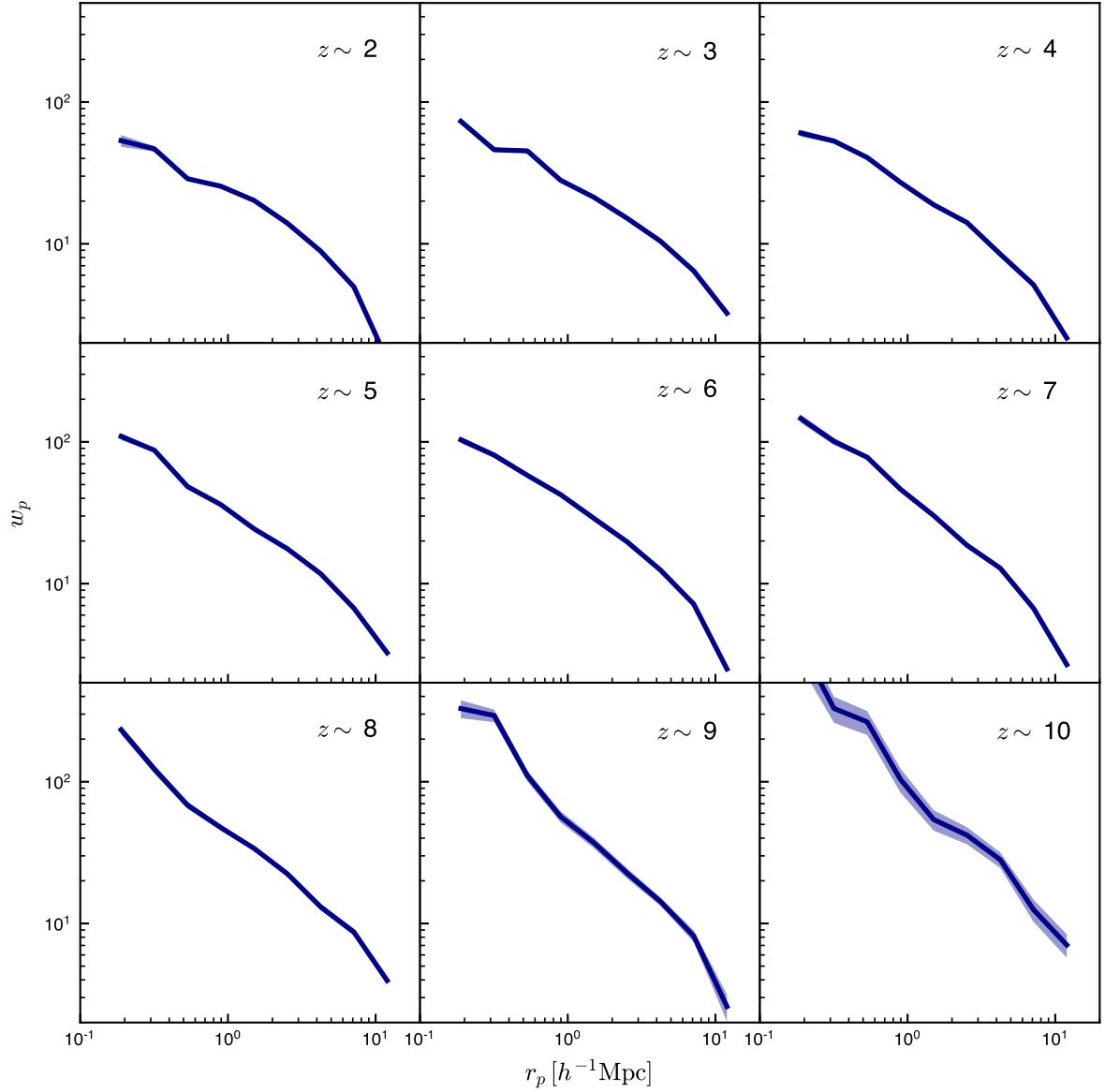
We create the synthetic images using GalSim (Rowe et al. 2015). GalSim contains a module specifically for *Roman* observations (Troxel et al. 2021), which includes five of the *Roman* filters: Z087, Y106, J129, H158 and F184. We model each galaxy as a Sérsic profile, with an index n_s, axis ratio q and PA, as described in Section 5. We truncate the distribution of Sérsic indices between 0.3 and 6.2, to avoid numerical inaccuracies at more extreme values. The scale radius of the Sérsic profile, r_0, is directly related to the assigned half-light radius, $R_{\rm eff}$:
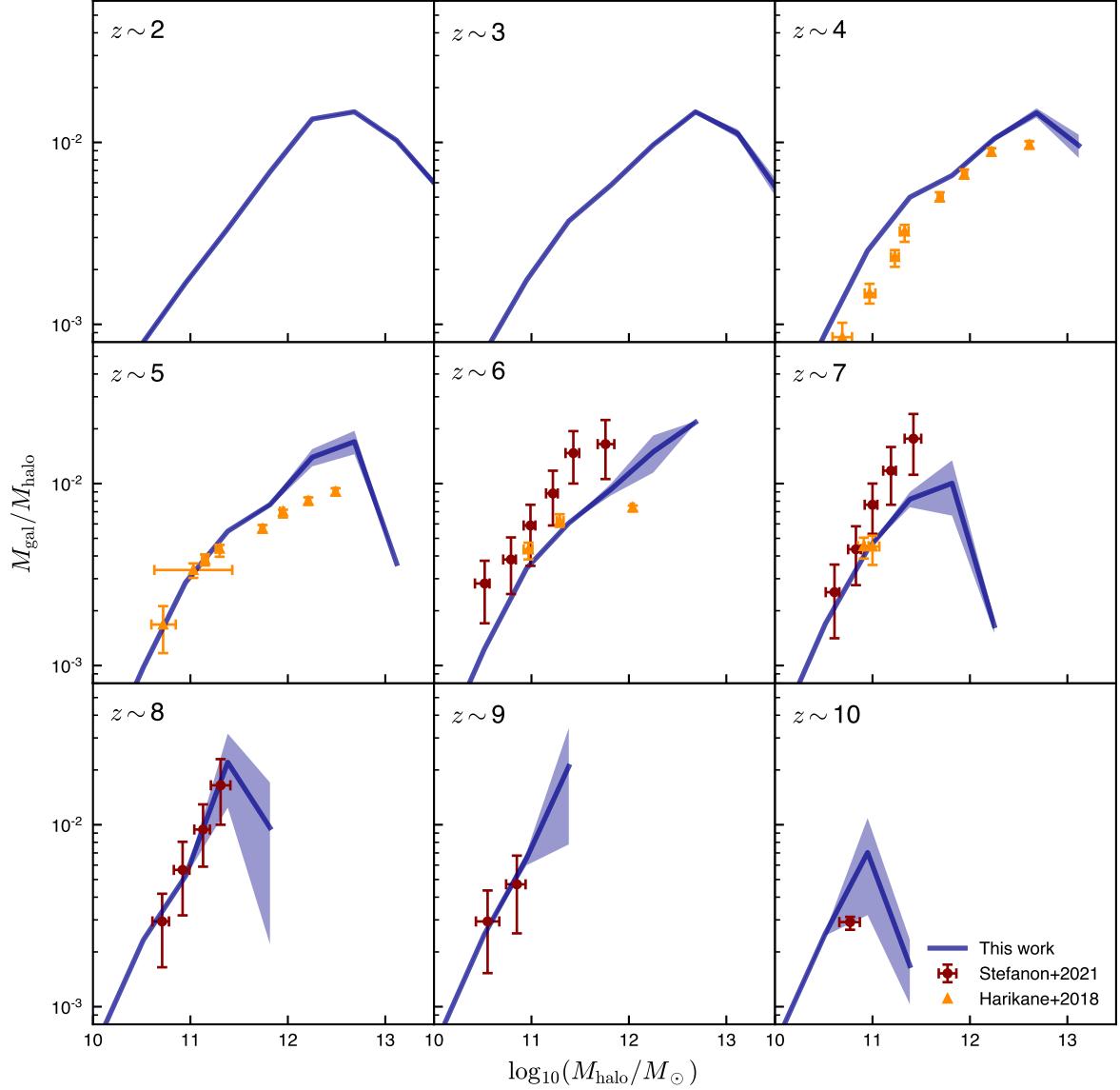
$$r_0 = \frac{R_{\rm eff}}{b^{n_s}\sqrt{q}} \ , \qquad (25)$$

where $b \approx 2n_s - 1/3$ (Moriondo et al. 1998). Fig. 21 shows a composite of the full synthetic galaxy catalog using Z087 (blue), Y106 (green), and H158 (red) filters.

Figure 18. The UVLF of the detectable galaxies in our synthetic galaxy catalog (blue lines) and the 1-σ Poisson noise (shaded region). We show the recent Bouwens et al. (2021) data for comparison (black points). We also indicate the number of sources, N, in each panel used to calculate the UVLF. A *Roman* UDF will provide remarkably tight constraints on the faint end of the UVLF at high redshifts.

Figure 19. The 2PCF of the $M_{\rm UV} < -18$ detectable galaxies in our synthetic galaxy catalog (blue lines), with the uncertainty calculated from bootstrapping the data. (shaded region). The 2PCF of the detectable galaxies is measured to within 1% for galaxies $z \lesssim 7$, and to within 10% at $z \approx 10$.

Figure 20. SHMR of the detectable galaxies in our synthetic galaxy catalog (blue solid line), and the 1σ spread (shaded blue region). We compare to data from Harikane et al. (2018) (orange points; error bars show error in the mean) and Stefanon et al. (2021) (red points; error bars denote the scatter). The Stefanon et al. (2021) data has been scaled by a factor of $1/1.7$ to convert to a Chabrier (2003) IMF. Stefanon et al. (2021) derived halo masses from abundance matching, while Harikane et al. (2018) derived halo masses from galaxy clustering data.

Table 4. Approximate exposure times for the simulated filters, as calculated in Koekemoer et al. (2019) to reach a 5σ limit of $m_{\rm AB} \approx 30$.

Filter	Exposure Time (hrs)
Z087	60
Y106	70
J129	90
H158	40
F184	60

We note that we do not include simulated stars in any of the released images.

To simulate a *Roman* 30 $m_{\rm AB}$ survey, we convolve the image with the *Roman* point spread function (PSF), and add noise to the image. We calculate the image noise assuming proposed exposure times from Koekemoer et al. (2019), to reach a 5σ limit of $m_{\rm AB} \approx 30$ (see Table 4). We add noise to the image in the same manner as Troxel et al. (2021). First, we generate the sky background accounting for the stray light and thermal emission from the telescope which is added to the image. Given this, we add errors associated with poisson noise, reciprocity failure, dark current, the calibration of the Roman detectors, inter-pixel capacitance, and instrument read noise.

We present a RGB visualization of the full *Roman* catalog, with the PSF and noise included in Fig 22, with one *Roman* footprint overlaid on top. Each *Roman* pointing will have 18 detectors. This visualization shows the rich amount of structure that will be contained in a *Roman* UDF. As described in Koekemoer et al. (2019), a $1\,{\rm deg}^2$ UDF would consist of three *Roman* pointings. Though a UDF based on three tiled WFI pointings would not be perfectly square, and the exposure time would not be perfectly uniform, these synthetic images demonstrate the richness of a $1\,{\rm deg}^2$ UDF and will be incredibly useful in designing and preparing for wide, deep surveys.

We include FITS maps of the galaxy catalog for all 5 filters currently included in GalSim in our data release. The top row of Fig. 23 shows the flux in one WFI detector (each detector has an area of $\sim 7.3' \times 7.3'$). The bottom row shows an example $z = 9.4$ galaxy (with the background subtracted in each panel). This galaxy would be selected as a Y106 dropout. The dropout galaxy has a size of $R_{\rm eff} = 0.38\,{\rm kpc}$, and therefore is not resolved with the WFI (which has an angular resolution of $0.11''$ per pixel).

The synthetic images we release are at the resolution of the WFI detector, $0.11''$ per pixel. An actual *Roman* UDF would likely be dithered, which would sample the sky on a sub-sampled pixel scale, which would im-

prove the PSF sampling and angular resolution. Since this process would create correlations between adjacent pixels, we did not include this in our data release. Future work will build upon DREaM to examine dithering strategies of a *Roman* UDF.

9. DISCUSSION
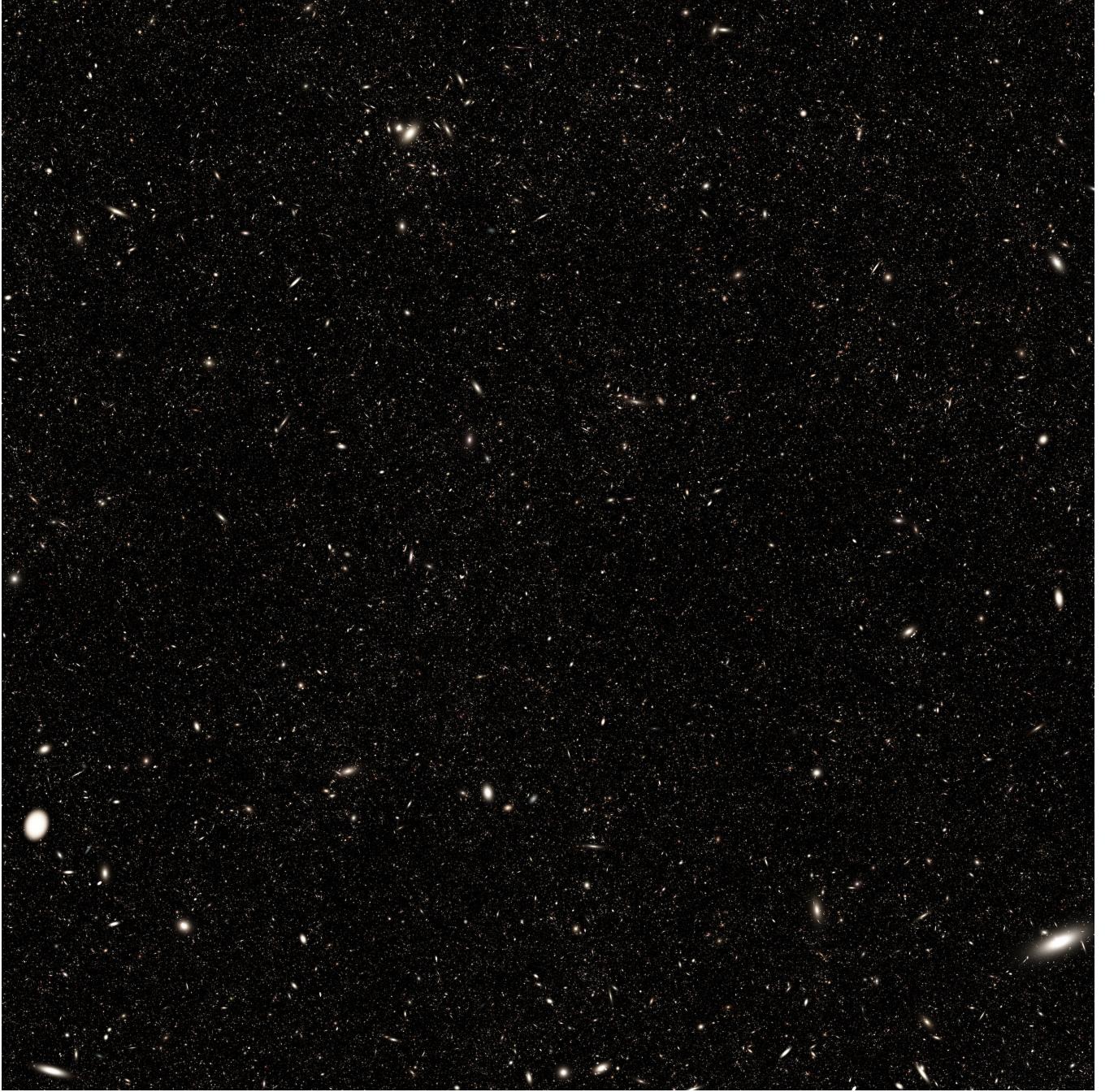
This work presents synthetic galaxy catalogs for a $1\,{\rm deg}^2$ UDF with *Roman*, created using DREaM, a model for deep, realistic realizations of galaxy populations. Our model successfully reproduces a number of well-known trends, including the size–mass relation, the fundamental metallicity relation, and UV luminosity functions. Additionally, we reproduce observed low-redshift galaxy clustering and SMFs. We have made the galaxy catalog, and synthetic images public, to provide the community tools to prepare for a potential UDF with *Roman*.

A UDF survey with *Roman* will address a number of science topics, including the EoR, the emergence of quiescent galaxies, and the high-redshift galaxy–halo connection. *Roman*'s large field of view will capture enormous sample sizes, over contiguous fields, imaging multiple ionization bubbles. This large area will decrease cosmic variance, and probe detailed environments around high-redshift galaxies.

9.1. *The epoch of reionization*

The EoR is the final frontier for galaxy surveys. Given the difficulty in measuring galaxies at high redshifts, this period in the universe's history is remarkably unconstrained. High-redshift low-mass galaxies were likely the major source of the ionizing photons in the EoR (e.g. Finkelstein et al. 2019), and observations indicate that reionization was a "patchy" process (e.g. Furlanetto & Oh 2005; Villasenor et al. 2021). To fully understand the EoR, we need a complete census of galaxies and their ionizing photon contribution.

To determine whether there are enough high-redshift, faint galaxies to cause reionization, we must accurately model the CSFRD, which depends on the UVLF. Though there are some constraints on the UVLF to $z \sim 10$ (e.g. Bouwens et al. 2021), there is still much improvement to be made on constraining both the bright steep end of the UVLF and the faint end (e.g. Bowler et al. 2014, 2015) at high redshifts. *JWST* will make improvements on this front. For example, Kauffmann et al. (2020) predicts that the $100\,{\rm arcmin}^2$ Cosmic Evolution Early Release Science Survey (CEERS), will constrain the faint-end of the UVLF to a precision of 0.25 at $z \geq 8$, but that a survey would need to be at least $300\,{\rm arcmin}^2$ to constrain bright end up to $z = 8$. We predict a *Roman* UDF will capture enough high-redshift galaxies to
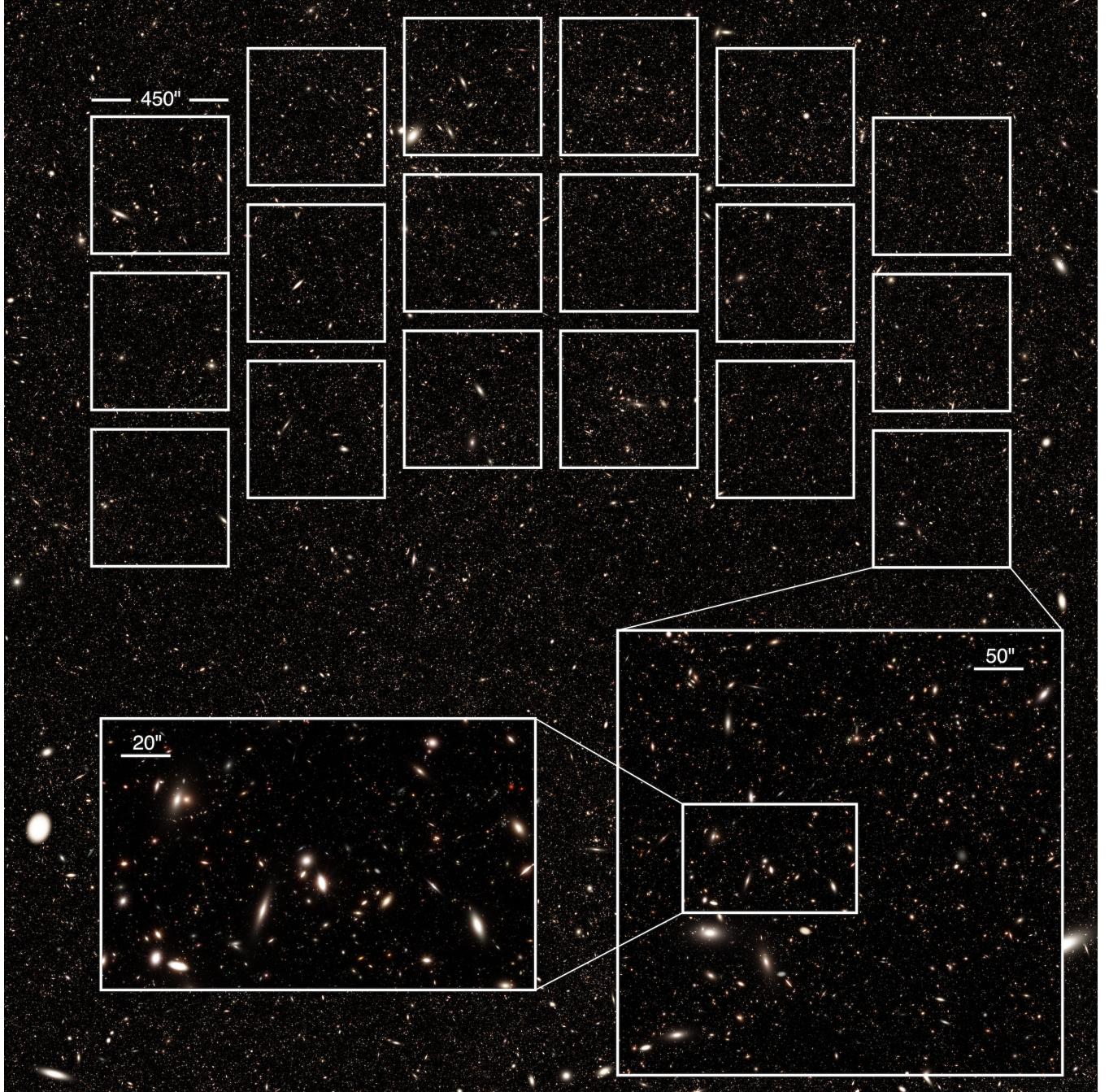
Figure 21. Noise-free composite simulated image of the full $1\,\mathrm{deg}^2$ galaxy catalog using the Z087 (blue), Y106 (green), and H158 (red) filters. The image was created with the *Roman* module in GalSim. A native resolution version is available online at https://www.nicoledrakos.com/dream.
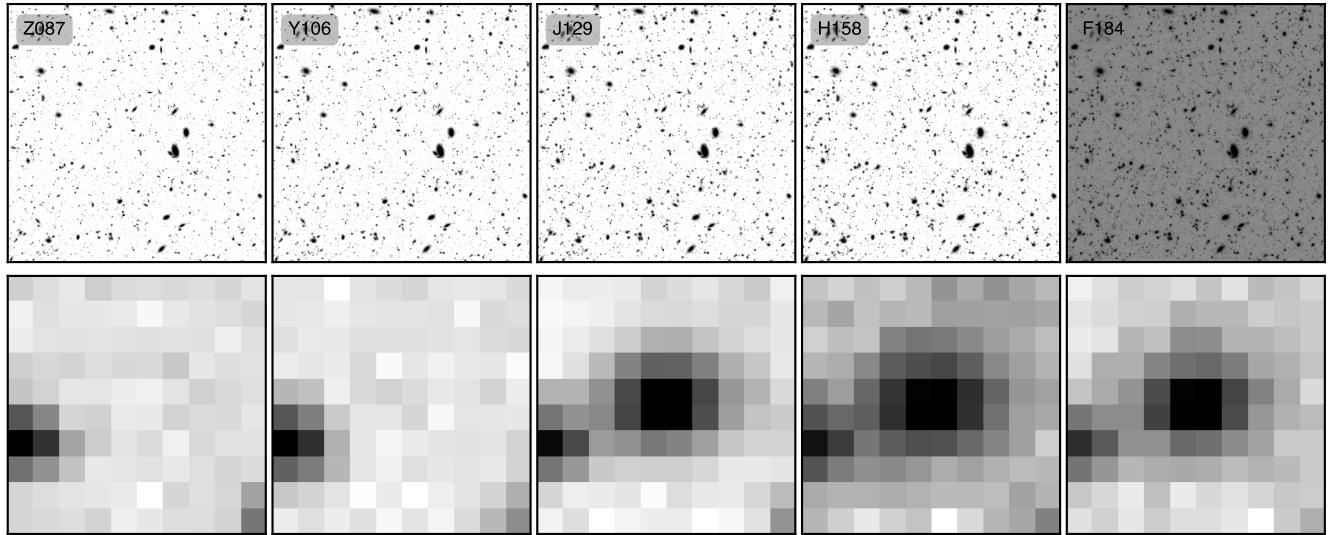
constrain the UVLF to within 1% at redshifts beyond $z \sim 10$. This will either confirm that there are enough faint galaxies to account for the ionizing photons needed to cause reionization, or indicate that another source, such as AGN (e.g. Madau & Haardt 2015) must contribute.

In addition to the abundance of galaxies, the total ionizing photon budget depends on the Lyman-continuum (LyC) production efficiency, ξ_{ion}, and the LyC escape fraction, f_{esc}. To account for reionization, galaxies need higher escape fractions at high redshifts than have been observed at low redshifts (Davies et al. 2021). Since the neutral IGM absorbs LyC photons, f_{esc} is very difficult to constrain at the EoR. However, f_{esc} could possibly be measured during the EoR using indirect methods (e.g. Leethochawalit et al. 2016; Zackrisson et al. 2017;

Figure 22. Composite simulated image of a region of the galaxy catalog using the Z087 (blue), Y106 (green), and H158 (red) filters convolved with the *Roman* PSF. Noise is calculated assuming a depth of $\sim 30\,m_{\mathrm{AB}}$ in each filter. The image was created with the *Roman* module in GALSIM. The *Roman* footprint is shown on top, as well insets showing a zoomed in region of the image. A native resolution version of this $1\,\mathrm{deg}^2$ visualization is available online at https://www.nicoledrakos.com/dream.

Figure 23. Flux in one WFI detector (top row), and an example of a Y106 dropout galaxy (bottom row). Each column corresponds to a different photometric filter, as labeled. The WFI detector has 4kx4k pixels, with an angular resolution of $0.11''$ per pixel. The example dropout galaxy is at redshift $z = 9.4$, has a galaxy mass of $M_{\mathrm{gal}} = 10^{7.6}\, M_{\odot}$.

Chisholm et al. 2018, 2020). A *Roman* UDF will detect tens of thousands of galaxies during the epoch of reionization, including rare, bright sources that are ideal for spectroscopic follow-up to measure f_{esc}. Further, since *Roman* can map out the density around each galaxy, it will allow for the measurement of the escape fraction in different environments.

9.2. *The emergence of quiescent galaxies*

There exists a clear bimodality in star formation rates, indicating two distinct populations (star-forming and quiescent). The decline in the CSFRD since redshift $z \approx 2$ was likely caused by the quenching of galaxies (e.g. Renzini 2016). However, the mechanisms that transforms galaxies from star-forming to quiescent are not fully understood. Possible mechanisms that have been proposed include feedback from stars and AGN, or the removal of gas through tidal or ram pressure stripping. Quenching is likely caused by a combination of these mechanisms, and the dominant processes may be redshift dependant (Kalita et al. 2021).

Advances in the understanding of the origin of quiescent galaxies is being greatly improved by surveys such as the spectroscopic survey Gemini Observations of Galaxies in Rich Early ENvironments (GOGREEN; Balogh et al. 2021), which targets quiescent galaxies in clusters around redshift $z \sim 1$. *Roman* has the potential to identify quiescent galaxy populations out to much higher redshifts. In particular, the synthetic catalog presented in this work predicts that an UDF with *Roman* will contain $\sim 10^5$ detectable quiescent galaxies, including QGs beyond redshift $z = 7$. Though the exact number of quiescent galaxies relies heavily on the underlying assumed SMF, *Roman* will likely detect the highest redshift QG to date if they exist, allowing for the study of quenching mechanisms at high redshifts.

9.3. *The galaxy–halo connection*

A *Roman* UDF will likely provide the first strong clustering measurements of the faint, high-redshift galaxies responsible for reionization, which will enable a measurement the underlying dark matter mass. In our preliminary predictions, we have shown that the coverage from a UDF will constrain the 2PCF for faint galaxies out to redshifts $z = 10$ (at the 10% level). These measurements will likely provide the first direct measurement of halo masses at $z = 10$, placing constraints the galaxy–halo connection at high redshift. Since the galaxy–halo connection depends on both galaxy formation physics and the underlying cosmological model, this will provide important tests for current models of galaxy formation.

9.4. *Synergies with JWST*

Roman's extensive field of view will allow for the contiguous, deep imaging of galaxies, reducing cosmic variance, and probe the environment around individual galaxies. The large number of galaxies detected by a *Roman* UDF will reduce poisson noise, and increase the number of rare objects that will be detected. Since a single *Roman* pointing is wide enough to capture several reionization bubbles at the height of reionization, a *Roman* UDF will allow for the study of differences between galaxies in ionized and neutral regions. For instance, there may be possible variations in the faint-end slope of the UVLF with environment, which can be measured with a deep, wide, galaxy survey.

Before the launch of *Roman*, *JWST* will begin to address questions regarding the EoR, galaxy formation and the galaxy–halo connection. In particular, the JWST Advanced Deep Extragalactic Survey (JADES) is a 236arcmin^2 planned imaging and spectroscopy survey[8] Though JADES will provide revolutionary data, it will detect less than $\sim 10\times$ the number of objects at all redshifts compared to a *Roman* UDF. In addition, cosmic variance may dominate over Poisson noise for future high-z surveys (Trapp & Furlanetto 2020), and JADES will cover a much smaller area.

Though *Roman* will cover a huge area on the sky, it will be difficult to obtain photometry at wavelengths greater than 2 microns. At high redshifts, accurate measurements of stellar masses and QG identification require supplementary imaging from another observing facility. *JWST* will probe very far into the infrared, which will potentially allow for Balmer-break selection of galaxies, improving redshift measurements and stellar mass estimates (though JWST is not sensitive to light blueward of 1 micron). Therefore, JWST may provide valuable spectroscopic followup to rare detections from a *Roman* UDF. For example, *Roman* will detect many galaxies, on the bright end of the UVLF. Bright galaxies (e.g. starburst galaxies, with $M_{UV} < -22$) are ideal for spectroscopic follow-up with JWST, and can be used to observe nebular lines and estimate f_{esc}.

9.5. *Applications of synthetic images*

In addition to the simulated galaxy catalog, we provide synthetic images of a *Roman* UDF. These images can be used to determine the impact of source blending, line confusion, potential problems with SED fitting

---

[8] Other JWST programs, such as Public Release IMaging for Extragalactic Research (PRIMER), and the COSMOS-Webb survey will cover larger areas than JADES, and probe the EoR, but neither will go as deep or as wide as a $1\,\mathrm{deg}^2$ *Roman* UDF.

(e.g. Borlaff et al. 2019; Massara et al. 2020; Kauffmann et al. 2020). Having very deep synthetic images will be useful for studying WFI systematics, processing issues (e.g. low surface brightness issues), and secondary analysis (e.g. photo-z studies). Quantifying these issues will also be beneficial for many other *Roman* surveys, such as the High Latitude Survey (HLS). For instance, in Section 8.1, we assumed that all galaxies that are detectable as will be selected. However, since a UDF will be so richly populated with structure, a fraction of the high redshift galaxies will be obscured by forefront galaxies. We intend to use the synthetic images and catalogs in this work to quantify this effect.

9.6. *Grism predictions*

In this paper we have only included photometric predictions, but the realistically modeled galaxy SEDs can also be used to generate grism predictions. In particular, the MOSFIRE Deep Evolution Field (MOSDEF) survey (Kriek et al. 2015) measured the detailed rest-frame optical emission-line SEDs in galaxies $z = 2$–3. More recent measurements with Keck/MOSFIRE have presented spectroscopic measurements out to $z \sim 8$ (Topping et al. 2021). We can combine these observations with our synthetic catalog, to guide the *Roman* grism data reduction pipeline at high redshifts.

The synthetic catalog can also be used to study Lyman-α emitters (LAEs). LAEs produce a large amount of ionizing photons, and both UVLFs and clustering of LAEs are important to characterize EoR. The Lyα UVLF decreases towards early stage of EoR, since neutral hydrogen absorbs Lyman-α photons (e.g. Ouchi et al. 2018). The clustering of LAEs emitters constrains the ionized fraction and topology of reionization.

10. SUMMARY AND CONCLUSIONS

This work presents DREaM, a Deep Realistic Extragalactic Model for creating synthetic galaxy catalogs. We use this model to understand the potential power of a $1 \deg^2$ UDF with *Roman*, and provide publicly available realistic synthetic galaxy catalogs and images. The synthetic catalogs and images will aid the community in designing and interpreting a *Roman* UDF. A summary of our main predictions are below.

A $1 \deg^2$ *Roman* UDF will:

1. contain more than 10^6 detectable galaxies, with more than 10^4 during the EoR ($z > 7$).

2. contain $\sim 10^5$ detectable quiescent galaxies, including a few at redshifts beyond $z \sim 7$, likely detecting the farthest redshift quiescent galaxy to date.

3. help constrain SMFs for SFGs to redshifts beyond $z \sim 10$, and for QGs past redshift $z \sim 7$.

4. provide tight constraints (within 1% percent) on the faint-end ($M_{UV} < -17$) of the UV luminosity function, out to redshifts $z \sim 10$.

5. provide high redshift ($z > 7$) constraints on the clustering of the faint galaxies thought to be responsible for reionization.

6. look for variations in the UVLF in different environments.

Overall, *Roman*'s wide field of view offers a unique ability to create wide, deep surveys. A *Roman* UDF would enable a tremendous amount of science by detecting the largest census of high-redshift galaxies to date, and differentiating between galaxy populations in low and high density regions during the EoR.

APPENDIX

A. DATA RELEASE

We have made a number of our data products public, as summarized in Table 5. We release a main galaxy catalog, a catalog containing intrinsic galaxy properties, and a halo catalog. The galaxy properties that are included in the catalogs are summarized in Table 6. These data products, and an interactive online visualization of the synthetic images are available at https://www.nicoledrakos.com/dream.

B. SYNTHETIC GALAXY PROPERTIES

Our main goal was to study the ability of a *Roman* UDF to constrain the photoionizing contribution of high redshift galaxies, and the environments around these galaxies. Therefore, we carefully constructed the DREaM galaxy catalogs to have realistic clustering properties and UV properties. In addition to these properties, our synthetic galaxies also capture a number of other observational trends.

In this section we examine some of the properties of the full galaxy catalog. We begin by looking at the how the UVJ colors (Section B.1), ages (Section B.3) and SFRs (Section B.2) differ between star-forming and quiescent galaxies. Additionally we verify that we reproduce the well-known fundamental metallicity relation (Section B.4).

B.1. *UVJ colors*

As discussed in Section 6.2.2, UVJ diagrams differentiate between star-forming and quiescent galaxy populations. We display the U-V and V-J colors for our two galaxy populations in Fig. 24, along with the UVJ selection box from Williams et al. (2009). The two populations occupy two distinct regions in this parameter space, demonstrating that the synthetic galaxy catalog does capture the bimodal population. Observational constraints for QGs do not currently exist for galaxies past redshifts $z \approx 4$, the UVJ distribution of the synthetic galaxies at low redshifts do agree with observations (e.g. Schreiber et al. 2015).

B.2. *Star formation rate*

We do not explicitly assign SFRs to the galaxies in the mock catalog, but we reproduce realistic trends in SFRs. By assigning realistic $M_{\rm UV}$ values to the SFGs, and constraining QGs to the appropriate place in the UVJ color diagrams, we accurately model a bimodal population, with SFGs having higher SFRs than QGs. Additionally

we reproduce the observed cosmic star formation rate density (CSFRD) as demonstrated in Section 7.2.

Fig. 25 shows the SFR–Mass relation of the synthetic catalog compared to the relations from Schreiber et al. (2017). We closely match the Schreiber et al. (2017) SFG SFR–mass relations. The SFRs for QGs is lower than the Schreiber et al. (2017) relation. However, the SFRs–mass relations from Schreiber et al. (2015) assumed that all IR emission from QGs originated from residual star-formation. Alternative explanation are that the IR emission originates from active galactic nuclei (AGN) torus emission, dust heating, or incorrect classification of SFGs. The QGs SFRs still agree with what current observations can predict.

B.3. *Age*

Galaxy ages are a measure of star-formation histories (SFHs). SFHs of individual galaxies, give a direct measurement of the evolution of different galaxy populations. Trends in galaxy ages have been well-established; for instance, QGs are older than SFGs, and high-redshift galaxies are older than low-redshift galaxies (e.g. Webb et al. 2020). However, galaxy ages for individual galaxies are difficult to measure due to degeneracies between other parameters (metallicity, dust), sensitivity to priors in fitting (e.g. Leja et al. 2019), and the similarity between SEDs in galaxies older than ~ 5 Gyr (e.g. Gallazzi et al. 2005). Our synthetic galaxy catalogs provide age estimates, and realistic SEDs to examine this further.

We calculate the mass-weighted age of the synthetic galaxies as

$$a_{\rm gal} = \frac{\int_0^{t_{\rm age}} (t_{\rm age} - t)\psi dt}{\int_0^{t_{\rm age}} \psi dt} \quad . \tag{B1}$$

For the delayed-tau model,

$$a_{\rm gal} = t_{\rm tot} - 2\tau + \frac{t_{\rm tot}^2}{\tau e^{t_{\rm tot}/\tau} - (\tau + t_{\rm tot})} \quad , \tag{B2}$$

where $t_{\rm tot} = t_{\rm age} - t_{\rm start}$ is the total time of star formation.
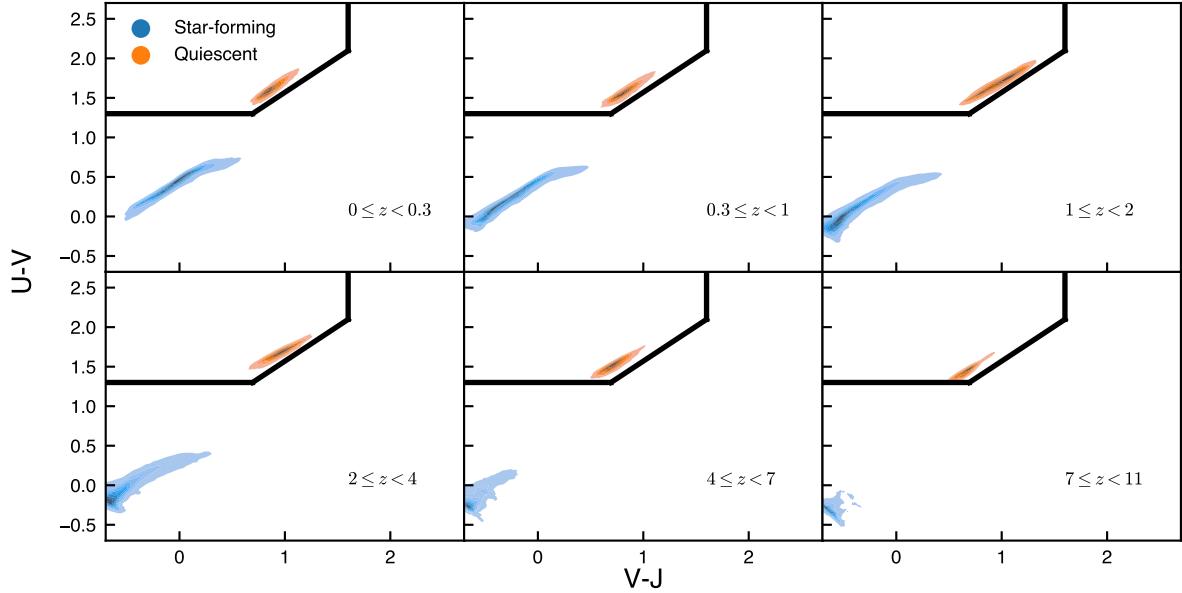
Fig. 26 shows the average galaxy ages as a function of redshift for both SFGs (blue) and QGs (red). QGs are older than SFGs at all redshifts and age decreases with increasing redshift, as expected. At low redshifts, QGs are ≈ 3 Gyr older than SFGs.

B.4. *Metallicity*

Galaxy metallicity can greatly affect quantities such as galaxy color, and therefore must be accurately modeled.

Table 5. Data Products. Available online at https://www.nicoledrakos.com/dream.

Product	Filename	Description
Main Catalog	`DREaM_main.fits`	Contains galaxy masses, positions, morphologies, rest-frame properties, and photometry in *Roman* and *JWST* filters. See Table 6 for more information.
Intrinsic Properties	`DREaM_intrinsic.fits`	Contains the FSPS parameters used to generate galaxy SEDs. See Table 6 for more information.
Halo Properties	`DREaM_halos.fits`	Contains the host halo properties, such as the mass, shape, size, spin and peculiar velocity of the host halos. See Table 6 for more information.
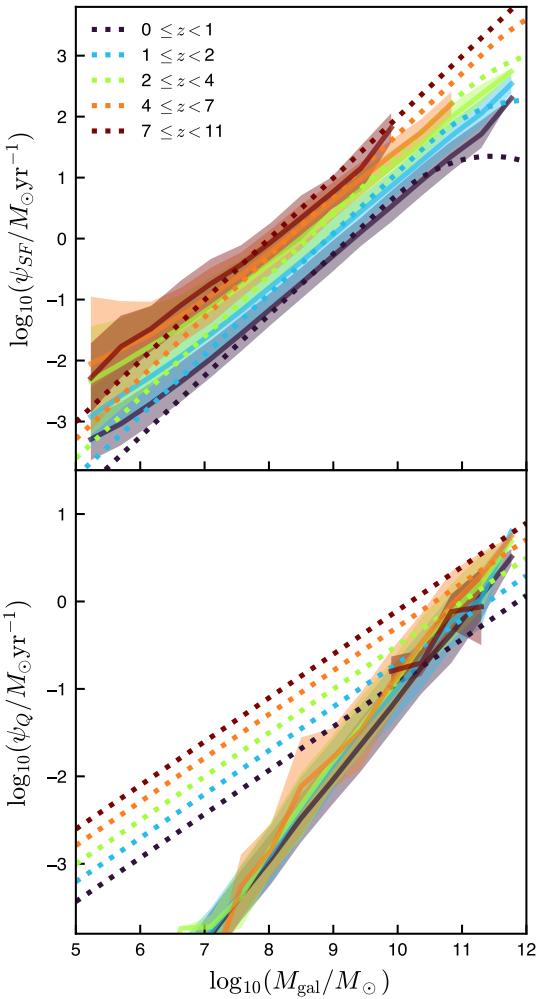
Figure 24. UVJ diagram of synthetic SFGs (blue) and QGs (orange). We used the selection box from Williams et al. (2009) (black lines). Our synthetic galaxies demonstrate a clear bimodal distribution, with SFGs falling in the top left corner of the UVJ diagram.

We assigned metallicities from the FMR (Equation 19, to the parent catalogs used in the SED pipeline. Fig. 27 shows the FMR for the synthetic galaxies. We show for comparison the FMR (dotted lines), where we have used the assumption $12 + \log_{10}(\text{O/H}) \approx \log_{10}(Z_{\text{met}}/Z_{\text{sol}})$.
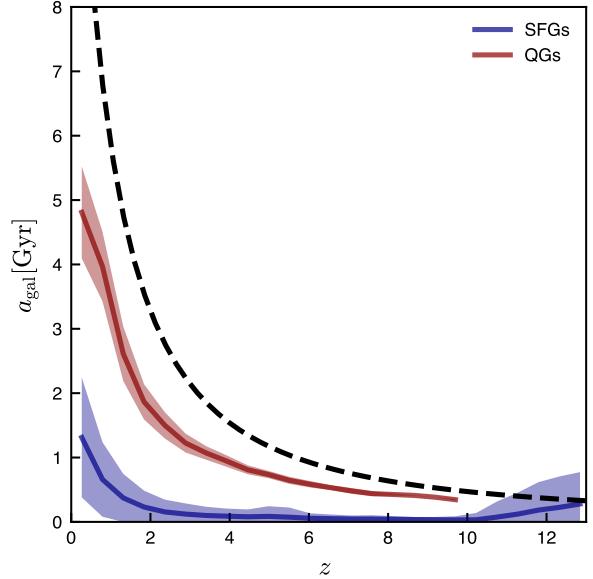
Our synthetic galaxies follow the expected FMR, where metallicity increases with mass, with a turn-over at high masses, as seen in observations (see discussion in Section 6.3). The low-mass galaxies have lower metallicities than the high-mass galaxies as expected, but do not vary much with SFR. However, at these low masses, very few galaxies will have SFRs $\psi > -1$.

Table 6. Catalog content. The galaxy information is contained in either the main catalog (MC), internal properties catalog (IPC) or halo properties catalog (HPC).
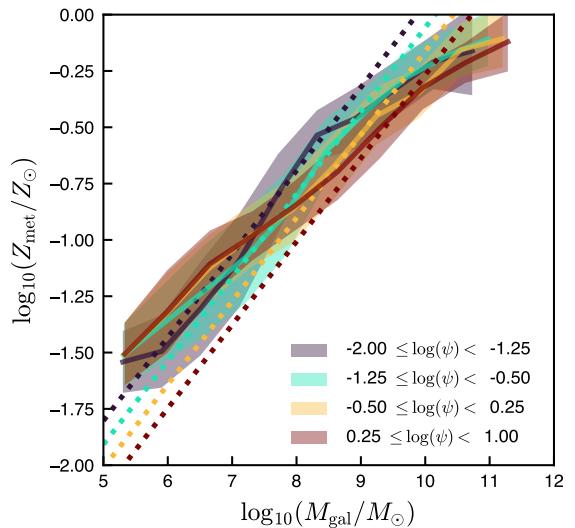
Variables	Description	MC	IPC	HPC
ID	Galaxy ID. The same across all the catalogs	✓	✓	✓
RA, Dec	Right Ascension and Declination [degrees, -0.5 to 0.5]	✓	✓	✓
redshift	Galaxy redshift	✓	✓	✓
M_halo	Halo mass [$M_\odot/h$]	✓	✓	✓
M_gal	Galaxy mass [$M_\odot$]	✓	✓	✓
logpsi	Star-formation rate [$\log_{10}(\psi/(M_\odot/\mathrm{yr}))$]	✓	✓	✓
M_UV	Rest-frame UV magnitude	✓	✗	✗
R_eff	Half-light radius in the semi-major axis [kpc/h, physical]	✓	✗	✗
n_s	Sérsic index	✓	✗	✗
q	Projected axis ratio: semi-minor to semi-major half-light size	✓	✗	✗
PA	Position angle [radians, 0 to 2π]	✓	✗	✗
beta	Rest-frame UV continuum slope	✓	✗	✗
U, V, J	Rest-frame magnitude in U, V and J bands	✓	✗	✗
R062, Z087, Y106, J129, H158, F184, F213	Apparent AB magnitude in *Roman* filters	✓	✗	✗
f070, f090, f115, f150, f200, f277, f356, f444	Apparent AB magnitude in *JWST* filters	✓	✗	✗
SF	Star-forming (True) or Quiescent (False)	✗	✓	✗
t_start	Age of universe when galaxy started forming [Gyr]	✗	✓	✗
tau	*e*-folding time for star formation [Gyr]	✗	✓	✗
logZ	Metallicity parameter [$\log_{10}(Z/Z_\odot)$]	✗	✓	✗
dust	Dust attenuation parameter	✗	✓	✗
logUS	Gas ionization parameter [$\log_{10}(U_s)$]	✗	✓	✗
V_max	Halo maximum circular velocity [km/s, physical]	✗	✗	✓
R_s	Halo scale radius [kpc/h, comoving]	✗	✗	✓
R_vir	Halo virial radius [kpc/h, comoving]	✗	✗	✓
M_peak	Halo peak mass over accretion history [$M_\odot/h$]	✗	✗	✓
V_peak	Halo peak $V_{\max}$ over accretion history [km/s, physical]	✗	✓	✗
b_a	Halo axis ratio, b/a	✗	✗	✓
c_a	Halo axis ratio, c/a	✗	✗	✓
haloID	ID of host halo	✗	✗	✓
hostID	ID of least massive host halo (-1 if distinct halo).	✗	✗	✓
spin_B	Bullock et al. (2001) halo spin parameter	✗	✗	✓
spin_P	Peebles (1971) halo spin parameter	✗	✗	✓
x,y,z	Halo positions [Mpc/h, comoving]	✗	✗	✓
vx,vy,vz	Halo peculiar velocities [km/s, physical]	✗	✗	✓

Figure 25. The average SFR versus galaxy mass for synthetic SFGs (top) and QGs (bottom). The SFRs increase with mass, and the SFGs have higher SFRs than QGs, as expected. For comparison, we plot the relation from Schreiber et al. (2017) (dotted lines). The galaxy catalog agrees closely with the Schreiber et al. (2017) parameterization for the SFGs. The QGs have lower SFRs than the Schreiber et al. (2017) parameterization, but are still consistent with observations (see discussion in text).

Figure 26. Average mass-weighted age of synthetic galaxies for SFGs (blue points) and QGs (red points), as defined in Equation (B1). QGS are older than SFGs, and ages decrease with increasing redshift. Galaxy ages are less than the age of the universe (dashed black line).

Figure 27. Mass–metallicity relation of the synthetic galaxies (solid lines). The shaded regions are one standard deviation. Dotted lines show the FMR from Williams et al. (2018), which were used to generate the parent catalog SEDs. The synthetic galaxies have increased metallicity with mass and SFR, in agreement with the underlying FMR.

REFERENCES

Abazajian, K. N., Adelman-McCarthy, J. K., Agüeros, M. A., et al. 2009, ApJS, 182, 543, doi: 10.1088/0067-0049/182/2/543

Astropy Collaboration, Robitaille, T. P., Tollerud, E. J., et al. 2013, A&A, 558, A33, doi: 10.1051/0004-6361/201322068

Astropy Collaboration, Price-Whelan, A. M., Sipőcz, B. M., et al. 2018, AJ, 156, 123, doi: 10.3847/1538-3881/aabc4f

Balogh, M. L., van der Burg, R. F. J., Muzzin, A., et al. 2021, MNRAS, 500, 358, doi: 10.1093/mnras/staa3008

Becker, G. D., Bolton, J. S., & Lidz, A. 2015, PASA, 32, e045, doi: 10.1017/pasa.2015.45

Beckwith, S. V. W., Stiavelli, M., Koekemoer, A. M., et al. 2006, AJ, 132, 1729, doi: 10.1086/507302

Behroozi, P., Wechsler, R. H., Hearin, A. P., & Conroy, C. 2019, MNRAS, 488, 3143, doi: 10.1093/mnras/stz1182

Behroozi, P., Conroy, C., Wechsler, R. H., et al. 2020, MNRAS, 499, 5702, doi: 10.1093/mnras/staa3164

Behroozi, P. S., Conroy, C., & Wechsler, R. H. 2010, ApJ, 717, 379, doi: 10.1088/0004-637X/717/1/379

Behroozi, P. S., Wechsler, R. H., & Wu, H.-Y. 2013a, ApJ, 762, 109, doi: 10.1088/0004-637X/762/2/109

Behroozi, P. S., Wechsler, R. H., Wu, H.-Y., et al. 2013b, ApJ, 763, 18, doi: 10.1088/0004-637X/763/1/18

Bell, E. F., van der Wel, A., Papovich, C., et al. 2012, ApJ, 753, 167, doi: 10.1088/0004-637X/753/2/167

Berlind, A. A., & Weinberg, D. H. 2002, ApJ, 575, 587, doi: 10.1086/341469

Bernyk, M., Croton, D. J., Tonini, C., et al. 2016, ApJS, 223, 9, doi: 10.3847/0067-0049/223/1/9

Blaizot, J., Wadadekar, Y., Guiderdoni, B., et al. 2005, MNRAS, 360, 159, doi: 10.1111/j.1365-2966.2005.09019.x

Borlaff, A., Trujillo, I., Román, J., et al. 2019, A&A, 621, A133, doi: 10.1051/0004-6361/201834312

Bouwens, R. J., Illingworth, G. D., Oesch, P. A., et al. 2014, ApJ, 793, 115, doi: 10.1088/0004-637X/793/2/115

—. 2015, ApJ, 803, 34, doi: 10.1088/0004-637X/803/1/34

Bouwens, R. J., Aravena, M., Decarli, R., et al. 2016, ApJ, 833, 72, doi: 10.3847/1538-4357/833/1/72

Bouwens, R. J., Oesch, P. A., Stefanon, M., et al. 2021, arXiv e-prints, arXiv:2102.07775. https://arxiv.org/abs/2102.07775

Bowler, R. A. A., Dunlop, J. S., McLure, R. J., et al. 2014, MNRAS, 440, 2810, doi: 10.1093/mnras/stu449

—. 2015, MNRAS, 452, 1817, doi: 10.1093/mnras/stv1403

Bryan, G. L., & Norman, M. L. 1998, ApJ, 495, 80, doi: 10.1086/305262

Bullock, J. S., Dekel, A., Kolatt, T. S., et al. 2001, ApJ, 555, 240, doi: 10.1086/321477

Bunker, A. J., Stanway, E. R., Ellis, R. S., & McMahon, R. G. 2004, MNRAS, 355, 374, doi: 10.1111/j.1365-2966.2004.08326.x

Byler, N., Dalcanton, J. J., Conroy, C., & Johnson, B. D. 2017, ApJ, 840, 44, doi: 10.3847/1538-4357/aa6c66

Calzetti, D., Armus, L., Bohlin, R. C., et al. 2000, ApJ, 533, 682, doi: 10.1086/308692

Campbell, D., van den Bosch, F. C., Padmanabhan, N., et al. 2018, MNRAS, 477, 359, doi: 10.1093/mnras/sty495

Carton, D., Brinchmann, J., Shirazi, M., et al. 2017, MNRAS, 468, 2140, doi: 10.1093/mnras/stx545

Chabrier, G. 2003, PASP, 115, 763, doi: 10.1086/376392

Charlot, S., & Fall, S. M. 2000, ApJ, 539, 718, doi: 10.1086/309250

Chisholm, J., Prochaska, J. X., Schaerer, D., Gazagnes, S., & Henry, A. 2020, MNRAS, 498, 2554, doi: 10.1093/mnras/staa2470

Chisholm, J., Gazagnes, S., Schaerer, D., et al. 2018, A&A, 616, A30, doi: 10.1051/0004-6361/201832758

Conroy, C., & Gunn, J. E. 2010, ApJ, 712, 833, doi: 10.1088/0004-637X/712/2/833

Conroy, C., Gunn, J. E., & White, M. 2009, ApJ, 699, 486, doi: 10.1088/0004-637X/699/1/486

Conroy, C., Wechsler, R. H., & Kravtsov, A. V. 2006, ApJ, 647, 201, doi: 10.1086/503602

Cortese, L., Catinella, B., & Smith, R. 2021, PASA, 38, e035, doi: 10.1017/pasa.2021.18

Cresci, G., Mannucci, F., & Curti, M. 2019, A&A, 627, A42, doi: 10.1051/0004-6361/201834637

Cucciati, O., Tresse, L., Ilbert, O., et al. 2012, A&A, 539, A31, doi: 10.1051/0004-6361/201118010

Curtis-Lake, E., McLure, R. J., Dunlop, J. S., et al. 2016, MNRAS, 457, 440, doi: 10.1093/mnras/stv3017

Davies, F. B., Bosman, S. E. I., Furlanetto, S. R., Becker, G. D., & D'Aloisio, A. 2021, arXiv e-prints, arXiv:2105.10518. https://arxiv.org/abs/2105.10518

DeRose, J., Wechsler, R. H., Becker, M. R., et al. 2019, arXiv e-prints, arXiv:1901.02401. https://arxiv.org/abs/1901.02401

—. 2021, arXiv e-prints, arXiv:2105.13547. https://arxiv.org/abs/2105.13547

Despali, G., Giocoli, C., Angulo, R. E., et al. 2016, MNRAS, 456, 2486, doi: 10.1093/mnras/stv2842

Diemer, B. 2018, ApJS, 239, 35, doi: 10.3847/1538-4365/aaee8c

Draine, B. T., & Li, A. 2007, ApJ, 657, 810, doi: 10.1086/511055

Duncan, K., Conselice, C. J., Mortlock, A., et al. 2014, MNRAS, 444, 2960, doi: 10.1093/mnras/stu1622

Dunlop, J. S. 2013, Observing the First Galaxies, Vol. 396 (Springer Science & Business Media), 223, doi: 10.1007/978-3-642-32362-1_5

Dunlop, J. S., McLure, R. J., Robertson, B. E., et al. 2012, MNRAS, 420, 901, doi: 10.1111/j.1365-2966.2011.20102.x

Endsley, R., Behroozi, P., Stark, D. P., et al. 2020, MNRAS, 493, 1178, doi: 10.1093/mnras/staa324

Evrard, A. E., MacFarland, T. J., Couchman, H. M. P., et al. 2002, ApJ, 573, 7, doi: 10.1086/340551

Finkelstein, S. L., Papovich, C., Ryan, R. E., et al. 2012, ApJ, 758, 93, doi: 10.1088/0004-637X/758/2/93

Finkelstein, S. L., Ryan, Russell E., J., Papovich, C., et al. 2015, ApJ, 810, 71, doi: 10.1088/0004-637X/810/1/71

Finkelstein, S. L., D'Aloisio, A., Paardekooper, J.-P., et al. 2019, ApJ, 879, 36, doi: 10.3847/1538-4357/ab1ea8

Finlator, K., Oppenheimer, B. D., & Davé, R. 2011, MNRAS, 410, 1703, doi: 10.1111/j.1365-2966.2010.17554.x

Foreman-Mackey, D., Sick, J., & Johnson, B. 2014, Python-Fsps: Python Bindings To Fsps (V0.1.1), v0.1.1, Zenodo, doi: 10.5281/zenodo.12157

Franx, M., van Dokkum, P. G., Förster Schreiber, N. M., et al. 2008, ApJ, 688, 770, doi: 10.1086/592431

Furlanetto, S. R., & Oh, S. P. 2005, MNRAS, 363, 1031, doi: 10.1111/j.1365-2966.2005.09505.x

Gallazzi, A., Charlot, S., Brinchmann, J., White, S. D. M., & Tremonti, C. A. 2005, MNRAS, 362, 41, doi: 10.1111/j.1365-2966.2005.09321.x

Girelli, G., Bolzonella, M., & Cimatti, A. 2019, A&A, 632, A80, doi: 10.1051/0004-6361/201834547

Gobat, R., Daddi, E., Magdis, G., et al. 2018, Nature Astronomy, 2, 239, doi: 10.1038/s41550-017-0352-5

Guo, H., Zehavi, I., Zheng, Z., et al. 2013, ApJ, 767, 122, doi: 10.1088/0004-637X/767/2/122

Guo, Y., Ferguson, H. C., Bell, E. F., et al. 2015, ApJ, 800, 39, doi: 10.1088/0004-637X/800/1/39

Hahn, O., & Abel, T. 2011, MNRAS, 415, 2101, doi: 10.1111/j.1365-2966.2011.18820.x

Harikane, Y., Ouchi, M., Ono, Y., et al. 2018, PASJ, 70, S11, doi: 10.1093/pasj/psx097

Harikane, Y., Ono, Y., Ouchi, M., et al. 2021, arXiv e-prints, arXiv:2108.01090. https://arxiv.org/abs/2108.01090

Harris, C. R., Millman, K. J., van der Walt, S. J., et al. 2020, Nature, 585, 357, doi: 10.1038/s41586-020-2649-2

Hearin, A. P., Zentner, A. R., Berlind, A. A., & Newman, J. A. 2013, MNRAS, 433, 659, doi: 10.1093/mnras/stt755

Hollowed, J. 2019, arXiv e-prints, arXiv:1906.08355. https://arxiv.org/abs/1906.08355

Hunt, L., Dayal, P., Magrini, L., & Ferrara, A. 2016, MNRAS, 463, 2002, doi: 10.1093/mnras/stw1993

Hunter, J. D. 2007, Computing in Science & Engineering, 9, 90, doi: 10.1109/MCSE.2007.55

Jiang, F., Dekel, A., Kneller, O., et al. 2019, MNRAS, 488, 4801, doi: 10.1093/mnras/stz1952

Jing, Y. P., Mo, H. J., & Börner, G. 1998, ApJ, 494, 1, doi: 10.1086/305209

Jo, Y., & Kim, J.-h. 2019, MNRAS, 2233, doi: 10.1093/mnras/stz2304

Kalita, B. S., Daddi, E., D'Eugenio, C., et al. 2021, arXiv e-prints, arXiv:2107.13241. https://arxiv.org/abs/2107.13241

Katz, N. 1992, ApJ, 391, 502, doi: 10.1086/171366

Katz, N., & Gunn, J. E. 1991, ApJ, 377, 365, doi: 10.1086/170367

Kauffmann, G., White, S. D. M., & Guiderdoni, B. 1993, MNRAS, 264, 201, doi: 10.1093/mnras/264.1.201

Kauffmann, G., White, S. D. M., Heckman, T. M., et al. 2004, MNRAS, 353, 713, doi: 10.1111/j.1365-2966.2004.08117.x

Kauffmann, O. B., Le Fèvre, O., Ilbert, O., et al. 2020, A&A, 640, A67, doi: 10.1051/0004-6361/202037450

Kikuchihara, S., Ouchi, M., Ono, Y., et al. 2020, ApJ, 893, 60, doi: 10.3847/1538-4357/ab7dbe

Kimm, T., Somerville, R. S., Yi, S. K., et al. 2009, MNRAS, 394, 1131, doi: 10.1111/j.1365-2966.2009.14414.x

Kitzbichler, M. G., & White, S. D. M. 2007, MNRAS, 376, 2, doi: 10.1111/j.1365-2966.2007.11458.x

Koekemoer, A., Foley, R. J., Spergel, D. N., et al. 2019, BAAS, 51, 550. https://arxiv.org/abs/1903.06154

Koekemoer, A. M., Ellis, R. S., McLure, R. J., et al. 2013, ApJS, 209, 3, doi: 10.1088/0067-0049/209/1/3

Korytov, D., Hearin, A., Kovacs, E., et al. 2019, ApJS, 245, 26, doi: 10.3847/1538-4365/ab510c

Kravtsov, A. V. 2013, ApJL, 764, L31, doi: 10.1088/2041-8205/764/2/L31

Kravtsov, A. V., Berlind, A. A., Wechsler, R. H., et al. 2004, ApJ, 609, 35, doi: 10.1086/420959

Kriek, M., Shapley, A. E., Reddy, N. A., et al. 2015, ApJS, 218, 15, doi: 10.1088/0067-0049/218/2/15

Landy, S. D., & Szalay, A. S. 1993, ApJ, 412, 64, doi: 10.1086/172900

Leethochawalit, N., Jones, T. A., Ellis, R. S., Stark, D. P., & Zitrin, A. 2016, ApJ, 831, 152, doi: 10.3847/0004-637X/831/2/152

Leethochawalit, N., Kirby, E. N., Moran, S. M., Ellis, R. S., & Treu, T. 2018, ApJ, 856, 15, doi: 10.3847/1538-4357/aab26a

Lehmann, B. V., Mao, Y.-Y., Becker, M. R., Skillman, S. W., & Wechsler, R. H. 2017, ApJ, 834, 37, doi: 10.3847/1538-4357/834/1/37

Leja, J., Carnall, A. C., Johnson, B. D., Conroy, C., & Speagle, J. S. 2019, ApJ, 876, 3, doi: 10.3847/1538-4357/ab133c

Lequeux, J., Peimbert, M., Rayo, J. F., Serrano, A., & Torres-Peimbert, S. 1979, A&A, 500, 145

Lotz, J. M., Koekemoer, A., Coe, D., et al. 2017, ApJ, 837, 97, doi: 10.3847/1538-4357/837/1/97

Ma, X., Hopkins, P. F., Boylan-Kolchin, M., et al. 2018, MNRAS, 477, 219, doi: 10.1093/mnras/sty684

Madau, P. 1995, ApJ, 441, 18, doi: 10.1086/175332

Madau, P., & Dickinson, M. 2014, ARA&A, 52, 415, doi: 10.1146/annurev-astro-081811-125615

Madau, P., & Haardt, F. 2015, ApJL, 813, L8, doi: 10.1088/2041-8205/813/1/L8

Mannucci, F., Cresci, G., Maiolino, R., Marconi, A., & Gnerucci, A. 2010, MNRAS, 408, 2115, doi: 10.1111/j.1365-2966.2010.17291.x

Massara, E., Ho, S., Hirata, C. M., et al. 2020, arXiv e-prints, arXiv:2010.00047. https://arxiv.org/abs/2010.00047

Meert, A., Vikram, V., & Bernardi, M. 2016, MNRAS, 455, 2440, doi: 10.1093/mnras/stv2475

Merlin, E., Fortuni, F., Torelli, M., et al. 2019, MNRAS, 490, 3309, doi: 10.1093/mnras/stz2615

Merson, A. I., Baugh, C. M., Helly, J. C., et al. 2013, MNRAS, 429, 556, doi: 10.1093/mnras/sts355

Meurer, G. R., Heckman, T. M., & Calzetti, D. 1999, ApJ, 521, 64, doi: 10.1086/307523

Miller, T. B., van Dokkum, P., Mowla, L., & van der Wel, A. 2019, ApJL, 872, L14, doi: 10.3847/2041-8213/ab0380

Mo, H. J., Mao, S., & White, S. D. M. 1998, MNRAS, 295, 319, doi: 10.1046/j.1365-8711.1998.01227.x

Mo, H. J., & White, S. D. M. 1996, MNRAS, 282, 347, doi: 10.1093/mnras/282.2.347

Moriondo, G., Giovanardi, C., & Hunt, L. K. 1998, A&AS, 130, 81, doi: 10.1051/aas:1998408

Mortlock, A., Conselice, C. J., Hartley, W. G., et al. 2013, MNRAS, 433, 1185, doi: 10.1093/mnras/stt793

Moster, B. P., Naab, T., Lindström, M., & O'Leary, J. A. 2020, arXiv e-prints, arXiv:2005.12276. https://arxiv.org/abs/2005.12276

Moster, B. P., Naab, T., & White, S. D. M. 2018, MNRAS, 477, 1822, doi: 10.1093/mnras/sty655

Mowla, L. A., van Dokkum, P., Brammer, G. B., et al. 2019, ApJ, 880, 57, doi: 10.3847/1538-4357/ab290a

Oesch, P. A., Bouwens, R. J., Illingworth, G. D., Labbé, I., & Stefanon, M. 2018, ApJ, 855, 105, doi: 10.3847/1538-4357/aab03f

Ouchi, M., Harikane, Y., Shibuya, T., et al. 2018, PASJ, 70, S13, doi: 10.1093/pasj/psx074

Papovich, C., Kawinwanichakij, L., Quadri, R. F., et al. 2018, ApJ, 854, 30, doi: 10.3847/1538-4357/aaa766

Peebles, P. J. E. 1971, Physical cosmology

Peng, Y., Maiolino, R., & Cochrane, R. 2015, Nature, 521, 192, doi: 10.1038/nature14439

Planck Collaboration, Aghanim, N., Akrami, Y., et al. 2018, arXiv e-prints, arXiv:1807.06209. https://arxiv.org/abs/1807.06209

Reddick, R. M., Wechsler, R. H., Tinker, J. L., & Behroozi, P. S. 2013, ApJ, 771, 30, doi: 10.1088/0004-637X/771/1/30

Reddy, N. A., & Steidel, C. C. 2009, ApJ, 692, 778, doi: 10.1088/0004-637X/692/1/778

Renzini, A. 2016, MNRAS, 460, L45, doi: 10.1093/mnrasl/slw066

Robertson, B. E., Ellis, R. S., Dunlop, J. S., McLure, R. J., & Stark, D. P. 2010, Nature, 468, 49, doi: 10.1038/nature09527

Robertson, B. E., Ellis, R. S., Furlanetto, S. R., & Dunlop, J. S. 2015, ApJL, 802, L19, doi: 10.1088/2041-8205/802/2/L19

Robertson, B. E., Furlanetto, S. R., Schneider, E., et al. 2013, ApJ, 768, 71, doi: 10.1088/0004-637X/768/1/71

Rowe, B. T. P., Jarvis, M., Mandelbaum, R., et al. 2015, Astronomy and Computing, 10, 121, doi: 10.1016/j.ascom.2015.02.002

Salpeter, E. E. 1955, ApJ, 121, 161, doi: 10.1086/145971

Schreiber, C., Pannella, M., Elbaz, D., et al. 2015, A&A, 575, A74, doi: 10.1051/0004-6361/201425017

Schreiber, C., Elbaz, D., Pannella, M., et al. 2017, A&A, 602, A96, doi: 10.1051/0004-6361/201629123

Shibuya, T., Ouchi, M., & Harikane, Y. 2015, ApJS, 219, 15, doi: 10.1088/0067-0049/219/2/15

Simha, V., Weinberg, D. H., Conroy, C., et al. 2014, arXiv e-prints, arXiv:1404.0402. https://arxiv.org/abs/1404.0402

Sinha, M., & Garrison, L. H. 2020, MNRAS, 491, 3022, doi: 10.1093/mnras/stz3157

Skelton, R. E., Whitaker, K. E., Momcheva, I. G., et al. 2014, ApJS, 214, 24, doi: 10.1088/0067-0049/214/2/24

Smith, A., Cole, S., Baugh, C., et al. 2017, MNRAS, 470, 4646, doi: 10.1093/mnras/stx1432

Somerville, R. S., & Davé, R. 2015, ARA&A, 53, 51, doi: 10.1146/annurev-astro-082812-140951

Somerville, R. S., & Primack, J. R. 1999, MNRAS, 310, 1087, doi: 10.1046/j.1365-8711.1999.03032.x

Somerville, R. S., Olsen, C., Yung, L. Y. A., et al. 2021, MNRAS, 502, 4858, doi: 10.1093/mnras/stab231

Spitler, L. R., Straatman, C. M. S., Labbé, I., et al. 2014, ApJL, 787, L36, doi: 10.1088/2041-8205/787/2/L36

Springel, V. 2005, MNRAS, 364, 1105, doi: 10.1111/j.1365-2966.2005.09655.x

Stark, D. P. 2016, ARA&A, 54, 761, doi: 10.1146/annurev-astro-081915-023417

Stark, D. P., Ellis, R. S., Bunker, A., et al. 2009, ApJ, 697, 1493, doi: 10.1088/0004-637X/697/2/1493

Stauffer, J., Helou, G., Benjamin, R. A., et al. 2018, arXiv e-prints, arXiv:1806.00554. https://arxiv.org/abs/1806.00554

Stefanon, M., Bouwens, R. J., Labbé, I., et al. 2021, arXiv e-prints, arXiv:2103.16571. https://arxiv.org/abs/2103.16571

Stefanon, M., Labbé, I., Bouwens, R. J., et al. 2017, ApJ, 851, 43, doi: 10.3847/1538-4357/aa9a40

Sérsic, J. L. 1968, Atlas de Galaxias Australes

Tasca, L. A. M., Le Fèvre, O., Hathi, N. P., et al. 2015, A&A, 581, A54, doi: 10.1051/0004-6361/201425379

Tomczak, A. R., Quadri, R. F., Tran, K.-V. H., et al. 2014, ApJ, 783, 85, doi: 10.1088/0004-637X/783/2/85

Topping, M. W., Shapley, A. E., Stark, D. P., et al. 2021, ApJL, 917, L36, doi: 10.3847/2041-8213/ac1a79

Trapp, A. C., & Furlanetto, S. R. 2020, MNRAS, 499, 2401, doi: 10.1093/mnras/staa2828

Tremonti, C. A., Heckman, T. M., Kauffmann, G., et al. 2004, ApJ, 613, 898, doi: 10.1086/423264

Troxel, M. A., Long, H., Hirata, C. M., et al. 2021, MNRAS, 501, 2044, doi: 10.1093/mnras/staa3658

Vale, A., & Ostriker, J. P. 2006, MNRAS, 371, 1173, doi: 10.1111/j.1365-2966.2006.10605.x

Valentino, F., Tanaka, M., Davidzon, I., et al. 2020, ApJ, 889, 93, doi: 10.3847/1538-4357/ab64dc

van den Bosch, F. C., More, S., Cacciato, M., Mo, H., & Yang, X. 2013, MNRAS, 430, 725, doi: 10.1093/mnras/sts006

van den Bosch, F. C., Yang, X., Mo, H. J., & Norberg, P. 2005, MNRAS, 356, 1233, doi: 10.1111/j.1365-2966.2004.08407.x

van der Wel, A., Rix, H.-W., Wuyts, S., et al. 2011, ApJ, 730, 38, doi: 10.1088/0004-637X/730/1/38

van der Wel, A., Bell, E. F., Häussler, B., et al. 2012, ApJS, 203, 24, doi: 10.1088/0067-0049/203/2/24

van der Wel, A., Franx, M., van Dokkum, P. G., et al. 2014, ApJ, 788, 28, doi: 10.1088/0004-637X/788/1/28

Villasenor, B., Robertson, B., Madau, P., & Schneider, E. 2021, ApJ, 912, 138, doi: 10.3847/1538-4357/abed5a

Villaume, A., Conroy, C., & Johnson, B. D. 2015, ApJ, 806, 82, doi: 10.1088/0004-637X/806/1/82

Virtanen, P., Gommers, R., Oliphant, T. E., et al. 2020, Nature Methods, 17, 261, doi: 10.1038/s41592-019-0686-2

Vogelsberger, M., Genel, S., Springel, V., et al. 2014, MNRAS, 444, 1518, doi: 10.1093/mnras/stu1536

Webb, K., Balogh, M. L., Leja, J., et al. 2020, MNRAS, 498, 5317, doi: 10.1093/mnras/staa2752

Wechsler, R. H., Bullock, J. S., Primack, J. R., Kravtsov, A. V., & Dekel, A. 2002, ApJ, 568, 52, doi: 10.1086/338765

Wechsler, R. H., DeRose, J., Busha, M. T., et al. 2021, arXiv e-prints, arXiv:2105.12105. https://arxiv.org/abs/2105.12105

Wechsler, R. H., & Tinker, J. L. 2018, ARA&A, 56, 435, doi: 10.1146/annurev-astro-081817-051756

Whitaker, K. E., van Dokkum, P. G., Brammer, G., et al. 2013, ApJL, 770, L39, doi: 10.1088/2041-8205/770/2/L39

White, S. D. M., & Frenk, C. S. 1991, ApJ, 379, 52, doi: 10.1086/170483

Williams, C. C., Curtis-Lake, E., Hainline, K. N., et al. 2018, ApJS, 236, 33, doi: 10.3847/1538-4365/aabcbb

Williams, R. J., Quadri, R. F., Franx, M., van Dokkum, P., & Labbé, I. 2009, ApJ, 691, 1879, doi: 10.1088/0004-637X/691/2/1879

Yang, X., Mo, H. J., van den Bosch, F. C., Zhang, Y., & Han, J. 2012, ApJ, 752, 41, doi: 10.1088/0004-637X/752/1/41

Yung, L. Y. A., Somerville, R. S., Finkelstein, S. L., Popping, G., & Davé, R. 2019a, MNRAS, 483, 2983, doi: 10.1093/mnras/sty3241

Yung, L. Y. A., Somerville, R. S., Finkelstein, S. L., et al. 2020a, MNRAS, 496, 4574, doi: 10.1093/mnras/staa1800

Yung, L. Y. A., Somerville, R. S., Popping, G., & Finkelstein, S. L. 2020b, MNRAS, 494, 1002, doi: 10.1093/mnras/staa714

Yung, L. Y. A., Somerville, R. S., Popping, G., et al. 2019b, MNRAS, 490, 2855, doi: 10.1093/mnras/stz2755

Zackrisson, E., Binggeli, C., Finlator, K., et al. 2017, ApJ, 836, 78, doi: 10.3847/1538-4357/836/1/78

Zanisi, L., Shankar, F., Lapi, A., et al. 2020, MNRAS, 492, 1671, doi: 10.1093/mnras/stz3516

Zehavi, I., Zheng, Z., Weinberg, D. H., et al. 2005, ApJ, 630, 1, doi: 10.1086/431891

Zu, Y., & Mandelbaum, R. 2015, MNRAS, 454, 1161, doi: 10.1093/mnras/stv2062